

1                                    Electronic Supplementary Information (ESI)  
2                                    **Engineering Polyvinyl Butyral-Hydrogel as Thermo-chromic**  
3                                    **Interlayer for Energy-Saving Window**

4                                    Zequn Lin<sup>1,2</sup>, Zican Yang<sup>1,2</sup>, Liang Gao<sup>1,2\*</sup>

- 5  
6 1. School of Chemical Engineering and Light Industry, Guangdong University of  
7 Technology, Guangzhou, 510006, P. R. China.  
8 Email: Liang Gao: [gaoliang@gdut.edu.cn](mailto:gaoliang@gdut.edu.cn);  
9 2. Jieyang Branch of Chemistry and Chemical Engineering Guangdong Laboratory  
10 (Rongjiang Laboratory), Jieyang 515200, P. R. China.

11

12

13

14

15

16

17

18

19

20

21

22

23

24

25

26

27

28

29

1 **Table of content:**

2 **I) General Materials and Methods**

3 **II) Supplementary Notes 1-11**

4 **III) Supplementary References**

5 **Descriptions on the Supplementary Videos**

6 **Video S1.** The distinct LCST phase transfer phenomenon of short alkyl side chains  
7 modified PVA analogies with identical degree of substitution: the PVA derivative with  
8 an octyl side chain exhibits a sluggish and irreversible phase transfer, whereas the PVA  
9 modified with a butyl side chain undergoes fast and reversible LCST phase transfer.

10 **Video S2.** Cyclic switches between opacity and transparent states: In this video, the  
11 FIRST hydrogel was sandwiched between a normal glass and an ITO glass, placed in a  
12 10°C environment. The ITO glass was heated using alternating currents at a frequency  
13 of 0.1 Hz, resulting in cyclic switches between the hydrogel's opacity and transparent  
14 states.

15 **Video S3.** The thermal response of the FIRST hydrogel-based thermochromic windows  
16 with phase transition being triggered by finger touch.

17

18

19

20

21

22

23

24

25

26

27

28

29

30

# I. General Materials and Methods

**Materials:** All reagents and solvents were used without further purification unless otherwise stated. Poly(vinyl alcohol) (PVA (99+% hydrolyzed );  $M_w$ : 146,000-186,000) was purchased from Sigma Aldrich. *n*-butanal, *N,N*-Dimethylformamide (DMF), sodium bicarbonate and acetonitrile were supplied by Macklin (China).

**Synthesis of kilogram-scale PVB with low acetalization degree:** 3 kg PVA was fully dissolved in 60 L water at 100 °C, followed by naturally cooling to 40 °C. Then, 0.91 L butyraldehyde was charged dropwise into the PVA solution and kept vigorous stirring for 4 h. Subsequently, the temperature of the reaction solution was cooled down to 10 °C, and then 0.25 L diluted sulfuric acid (10 wt.%) was added dropwise to initiate the acetylation. After stirring for approximate 3 hours, a milky suspension was produced and poured into excessive amount of saturated sodium bicarbonate solution with pH=8 to immediately terminate the reaction. Then, the suspension was filtrated, and the filter cake was collected. After intensively washing with 50 °C DI water, the powder was dried under 45 °C.

**FIRST hydrogel:** PVB was prepared according to the procedure outlined above and subsequently dissolved in DMF or DMSO at a concentration of approximately 8-10 wt%. The resulting clear solutions were injected into a glass mold with a uniform depth of approximately 3 mm. These molds were left exposed to a low relative humidity environment (~13%) until a constant weight was achieved. During our series of trial experiments, maintaining the atmospheric temperature at approximately 50°C, we successfully obtained a clean and smooth film 0.3 mm within 48 hours. This freshly fabricated film was then subjected to equilibration in LiCl solution (10 wt%) at around 20°C, resulting in the desired FIRST hydrogel of 0.3 mm. Note that the depth of injected liquids can be varied to achieve samples with different thickness.

**General physical characterizations: Nuclear Magnetic Resonance (NMR).** The NMR spectrum of C4-0.3 was recorded by using  $d_6$ -DMSO as the solvent on a Bruker 400 MHz spectrometry. **Gel Permeation Chromatography (GPC).** GPC measurements were carried out in DMF with 0.1 M LiBr at 60 °C with the Agilent 1260 Infinity II instrument, equipped with PLgel 10  $\mu$ m MIXED-B columns, and a

1 differential refractive index (DRI) detector. The system was calibrated with poly( $\gamma$ -  
2 benzyl-L-glutamate) standards at a flow rate of 1.0 mL/min. **Fourier transform**  
3 **infrared spectra (FTIR)**. The bonding information of the solid-state dry FIRST gel  
4 and PVA semi-crystalline was studied using a Nicolet 6700 with an attenuated total  
5 reflection (ATR) accessory (resolution: 4  $\text{cm}^{-1}$ ). **Differential scanning calorimeter**  
6 **(DSC)**. The changes in intermolecular cohesion after PVA grafting of butyraldehyde  
7 side chains were investigated by DSC (Q20, TA, America) at a rate of 10  $^{\circ}\text{C}/\text{min}$  from  
8  $-30^{\circ}\text{C}$  to  $125^{\circ}\text{C}$  under  $\text{N}_2$  flow (30 ml/min). **Scanning electron microscope (SEM)**.  
9 The image of FIRST hydrogels is completed by the steps of equilibrating at the  
10 corresponding temperature, quickly putting them into a locked state in liquid nitrogen,  
11 and finally taking them under a scanning electron microscope (SU8220, Hitach, Japan).  
12 **Rheological test**. The temperature ramp test and the oscillation sweep test were carried  
13 out in the rheometer (ares-g2, TA, America). In the temperature ramp test, the strain ( $\gamma$ )  
14 is 1% and the heating rate is 1 K/min. The temperature range is  $-15$ - $40^{\circ}\text{C}$ , and the  
15 number of cycles is 1. the test temperature is  $-15^{\circ}\text{C}$ ,  $20^{\circ}\text{C}$  and  $40^{\circ}\text{C}$ , and the scanning  
16 time is 600s. A disk-shaped sample with a diameter of 25.0 mm and a thickness of 0.5  
17 mm was fixed between plain metal plates. To prevent water evaporating from the gel,  
18 the sample was surrounded by water during the measurement. **Raman spectroscopy**.  
19 The samples were tested on a confocal Raman spectrometer equipped with a heated and  
20 cooled stage (LabRAM HR Evolution, HORIBA Jobin Yvon, France), using a 785 nm  
21 laser for excitation, an integration time of 60 s, and a cycle number of 1. The process  
22 adopts a heating rate of 1 K/min and a stabilization time of 20 min. The collected  
23 spectral data is processed with Labspec software. **Differential Scanning Calorimetry**.  
24 DSC measurement was conducted on a DSC 214 (DSC3). 5-10 mg hydrogel sample  
25 was collected in the aluminum pan, and an empty pan was used as reference. All  
26 hydrogel samples were equilibrated at  $15^{\circ}\text{C}$  for 5 min, ramped at  $2^{\circ}\text{C}/\text{min}$  to  $40^{\circ}\text{C}$   
27 under nitrogen atmosphere. **Mechanical test**. Tensile test was performed with a  
28 hydrogel sample with a length of 20 mm, width of 8 mm and thickness of 300  $\mu\text{m}$  at  
29 high temperature, room temperature and low temperature (i.e.  $40$ ,  $25$ ,  $-15^{\circ}\text{C}$ ).  
30 Rectangular sheets of hydrogel samples were fixed to two fixture and mounted in an  
31 Inspekt Table Blue 5KN tension tester with a 500 N load cell, with ambient temperature  
32 controlled by an environmental chamber supplied with liquid nitrogen.

## II. Supplementary Notes

### Supplementary Note 1. Summary on reported hydrogel systems related to this work.

As laminate for thermochromic windows, the majority of thermosensitive hydrogels currently in use are created through covalently crosslinking assorted monomers and crosslinking reagents. Despite great progress, these systems suffer from several drawbacks. For example, although an aqueous dispersion of LCST microgels undergo fast and uniform LCST phase separation, and flow to fit arbitrary shape of windows,<sup>1,2</sup> but they are prone to leak when the glass cracks. Also, the suspension of aggregated polymers is susceptible to precipitate upon chromic setting, leading to the failure in optical shielding. Bulk hydrogels can circumvent these issues, but they typically experience significant reduction in volume after undergoing a phase transition (refer to **Tables S1-S2**). Additionally, most isochoric LCST hydrogels tend to stiffen when exposed to heat, which hampers their ability to relax and flow, thus limiting their thermal processability and potential for recovery.

**Table S1.** Crosslinking types and syneresis during phase transition for several typical LCST and UCST hydrogels that potentially useful for thermochromic windows.

Thermal response type	Hydrogel	Crosslinking	Volume shrinkage <sup>a</sup>	Reference <sup>c</sup>
LCST	PNIPAM	Covalent crosslinking	Significant syneresis (present in Figure S4 in the cited paper)	3
	P(NIPAM- <i>co</i> -DMAA)	Covalent crosslinking	No significant syneresis	
	PNIPA-PDMA	Covalent crosslinking	No significant syneresis	4
	PNIPAM-PDMA	Covalent crosslinking	No significant syneresis	5
	PNIPAM/POSS hybrid	Covalent crosslinking	Significant syneresis (present in Figure 5 in the cited paper)	6
	PNIPAM/VO <sub>2</sub>	Covalent crosslinking	NA <sup>b</sup>	7

	PNIPAM/VO <sub>2</sub> @SiO <sub>2</sub>	Covalent crosslinking	NA	8
	PNIPAM/PEG	Covalent crosslinking	Significant syneresis (about 37%- as present in Figure 5 in the cited paper)	9
	PNIPAM/PEG/PANI	Covalent crosslinking	Significant syneresis (about 37-50% as present in Figure 5 in the cited paper)	
	PNIPAM-GO	Covalent crosslinking	Significant syneresis (about 40-65% as present in Figure 5 in the cited paper)	10
	PNIPAM-HPC composite	Covalent crosslinking	Not significant	11
	H-ESO-HEC/poly(NVCL- <i>co</i> -DMAA)	Covalent crosslinking	Significant syneresis (about 86% as present in Figure 5a in the cited paper)	12
	Poly ( <i>N</i> -isopropylacrylamide- <i>co</i> -acryloylaminozaobenzene,	Covalent crosslinking	Significant syneresis (about 94-96% as present in Figure 1 in the cited paper)	13
	PAAc/CaAc	Covalent crosslinking	Not significant	14
	PU/POSS	Covalent crosslinking	No significant shrinkage but obvious deformation upon heating (as present in Figure 2a in the cited paper)	15
	PNVCL	Covalent crosslinking	Significant syneresis (about 72% as present in Figure 7 in the cited paper)	16
	PNVCL-Clay composite	Physical crosslinking (Clay surface)	Significant syneresis (about 77%-83% as present in Figure 7 in the cited paper)	
	HPC imbedded within PAM-PAA	Covalent crosslinking	Not significant	17
	EGP5/ATO	Covalent crosslinking	Not significant	18
UCST	PAAm-SDS	Covalent crosslinking	Not significant	19
	PAAm-SDS-PTH	Covalent	NA <sup>a</sup>	20

		crosslinking		
	PAAm-SDS-LiCl	Covalent crosslinking	NA <sup>a</sup>	21
	PAAm-SDS- NaCl		Not significant	
	PAAm-SDS- KCl		NA <sup>a</sup>	
	PEG/PAAm- SDS-PTH	Covalent crosslinking	NA <sup>a</sup>	22

1 <sup>a</sup> The volume shrinkage percentage is defined as  $1-(V_{T>LCST}/V_0)$ , where  $V_{T>LCST}$  and  $V_0$  are the volume  
2 of hydrogel. In some literatures, the volume shrinkage percentage was not qualitatively provided.

3 <sup>b</sup> No available data was reported in relevant literature. The information about these LCST-type hydrogel  
4 systems is partially sourced from various recent reviews focusing on "hydrogel smart windows"<sup>8, 23</sup>.

5 <sup>c</sup> Please be aware that the cited references may not directly address the application of thermochromic  
6 windows. However, it is worth noting that the LCST hydrogels developed in these studies have the  
7 potential to serve as effective laminates for thermochromic windows.

8 **Table S2.** Isochoric LCST hydrogels with thermally-induced stiffening effect.

Hydrogel	Crosslinking	Thermally induced stiffening	Reference <sup>b</sup>
PNIPAM-PDMA	Covalent crosslinking	Yes	4
PNIPAM-PDMA	Covalent crosslinking	Yes	
PAAc/CaAc	Covalent crosslinking	Yes	14
PNIPAM-PDMA	Covalent crosslinking	Yes	5
EGP5/ATO	Covalent crosslinking	NA <sup>a</sup>	18

9 <sup>a</sup> No available data was reported in relevant literature. The information about these LCST-type hydrogel  
10 systems is partially sourced from various recent reviews focusing on "hydrogel smart windows"<sup>8, 23</sup>.

11 <sup>b</sup> Please be aware that the cited references may not directly address the application of thermochromic  
12 windows. However, it is worth noting that the LCST hydrogels developed in these studies have the  
13 potential to serve as effective laminates for thermochromic windows.

14

15

16

17

18

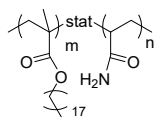
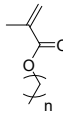
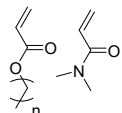
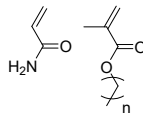
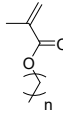
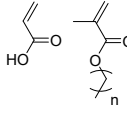
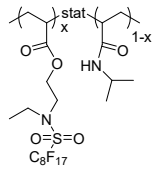
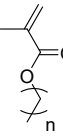
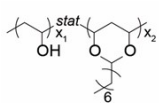
19

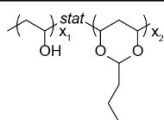
20

21

1 **Table S3** specifically examines hydrophobically modified hydrogels in their fully  
 2 swollen state. We also note that some hydrophobically modified hydrogels are created  
 3 through micellar copolymerization, which involves the use of surfactants to facilitate  
 4 the dispersion and dissolution of the hydrogels <sup>20</sup>. Due to the effective dispersion of  
 5 hydrophobic clusters, some of these gels demonstrate high transparency in their initial  
 6 state. However, it remains uncertain whether this transparency will be maintained when  
 7 the gels are equilibrated in water.

8 **Table S3.** Typical hydrophobic association hydrogels and their optical properties

Side alkyl chains	Average number of carbon atoms	Transparency	References
	18	Opaque, Semi-transparent	24
	18 or 22	Opaque, transparent	25
	18	Opaque	26
	16	Opaque	27
	17.3 or 18	Opaque	28
	18	Opaque	29
	~10	Semi-transparent	30
	18	Opaque	31
	8	Transparent	32, 33



4

Transparent

This work

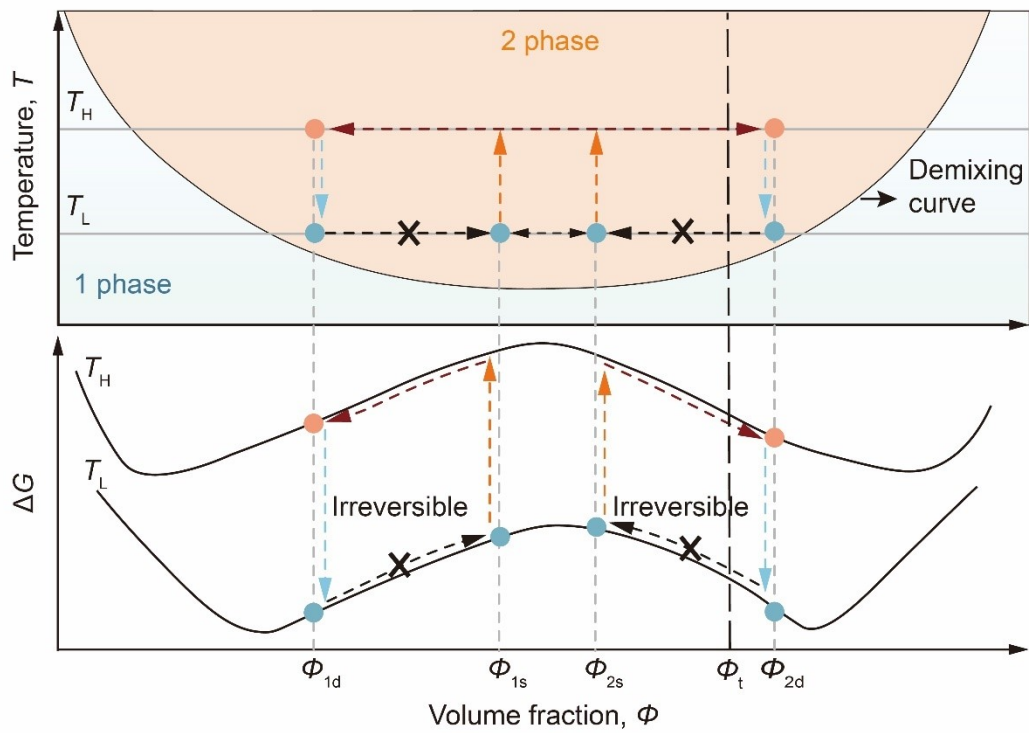
---

- 1
- 2
- 3
- 4
- 5
- 6
- 7
- 8
- 9
- 10
- 11
- 12
- 13
- 14
- 15
- 16
- 17
- 18
- 19
- 20
- 21
- 22
- 23
- 24
- 25
- 26
- 27
- 28
- 29
- 30
- 31
- 32
- 33
- 34
- 35
- 36
- 37
- 38
- 39

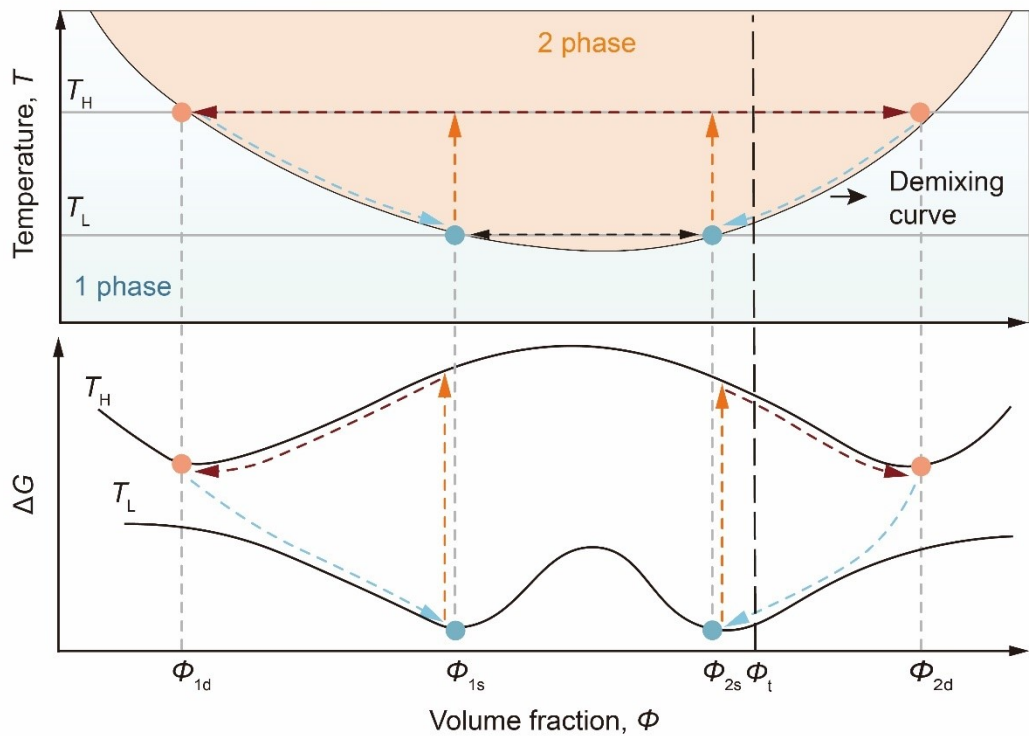
1 **Supplementary Note 2. Phase diagram of hydrophobically modified hydrogels**  
2 **and the reversibility of their LCST phase transfer.**

3 LCST behavior can be described as the thermally induced demixing of one  
4 homogeneous phase into two phases: one phase consists of a low polymer fraction ( $\Phi_1$ )  
5 (or even pure water), and the other phase has a high polymer fraction ( $\Phi_2$ ).  
6 Thermodynamically, a phase diagram in **Figure S1** is commonly used to delineate the  
7 relations between temperature ( $T$ ) and the composition of polymer-water mixtures ( $\Phi$ ).  
8 Phenomenally, the phase transition is straightforward to characterize: the cloud point  
9 describes a characteristic change in turbidity upon the formation of polymer aggregates  
10 large enough (with fraction of  $\Phi_t$ ) to scatter light.

**a** Conventional Hydrophobically modified hydrogel (irreversible phase transition)



**b** FIRST hydrogel (reversible phase transition)



1  
 2 **Figure S1. Phase diagram coupled with the Gibbs free energy to illustrate the**  
 3 **partially irreversible (a) and fully reversible (b) LCST phase transfer.** The phase  
 4 diagram depicts the temperature ( $T$ , vertical coordinate) vs. polymer–water composition  
 5 ( $\Phi$ ) (horizontal coordinate) phase diagram with upper miscibility gap. The position of

1 the demixing line is indicated, which set a boundary between homogeneous region  
 2 (shadowed with gradient grey color) and demixing region (shadowed with gradient  
 3 orange color). In this diagram, the colorful circles (●○) represent the  $T$ - $\Phi$  point of  
 4 different states of the hydrogel. The initial state can be in out-of-the equilibrium (in **a**)  
 5 or equilibrium state (in **b**). The initial temperature is set as  $T_L$ , the polymer rich and  
 6 polymer poor phase in initial gel has the compositions of  $\Phi_{1s}$  and  $\Phi_{2s}$ , respectively.  
 7 Thus, the circles of ● locate at  $(T_L, \Phi_{1s})$  and  $(T_L, \Phi_{2s})$  in two phase regions with shallow  
 8 phase separation depth. This state is in out-of-the equilibrium state (in **a**) or in  
 9 equilibrium state (in **b**). During hydrothermal treatment, the temperature of the  
 10 hydrogel jumps from  $T_L$  to  $T_H$  (represented by the orange arrow), shifting the state at  
 11  $(T_L, \Phi_{1s})$  and  $(T_L, \Phi_{2s})$  to  $(T_H, \Phi_{1s})$  and  $(T_H, \Phi_{2s})$ . As the hydrogel is aged in hot water  
 12 (represented by the red arrow), its composition gradually approaches the binodal line  
 13 and experiences time-dependent pore growth due to the slow dynamics of the polymer-  
 14 rich phase (which is close to vitrification). For example, after aging in hot water, the  
 15 state at  $(T_H, \Phi_{1s})$  and  $(T_H, \Phi_{2s})$  shifts to  $(T_H, \Phi_{1d})$  and  $(T_H, \Phi_{2d})$  (as indicated by ●) with  
 16 relatively deeper phase separation depth. In **a**, after cooling from  $T_H$  to  $T_L$  (represented  
 17 by the green arrow), the state  $(T_H, \Phi_{1d})$  and  $(T_H, \Phi_{2d})$  points become  $(T_L, \Phi_{1d})$  and  $(T_L,$   
 18  $\Phi_{2d})$  without alternation on compositions of two phases, suggesting the irreversibility  
 19 of the hydrothermally induced phase separation. The phase diagram is correlated with  
 20 a graph describing its Gibbs free energy vs. composition to formulate the reversibility  
 21 of the hydrothermally induced phase separation. Clearly, the morphology formed at  $T_H$   
 22 can be retained as the temperature lowers from  $T_H$  to  $T_L$  (represented by the green  
 23 arrow), due to the reduction in Gibbs energy ( $\Delta G < 0$ ). The cloud line corresponds to a  
 24 critical fraction of polymer-rich phase ( $\Phi_c$ ). When the fraction of polymer-rich phase  
 25 ( $\Phi_2$ ) in a gel exceeds  $\Phi_t$ , the gel turns turbid.

26 In principle, the LCST phase diagram can be modeled theoretically *via* Flory–Huggins  
 27 solution theory within the liquid–liquid equilibrium thermodynamic framework.<sup>34</sup> This  
 28 theory constitutes a set of  $\Delta G$  (Gibbs free energy)- $\Phi$  curves (**Figure S1**). At a given  
 29 temperature, the formed two phases have two extreme points at specific  $\Phi$  points. These  
 30 points stand for the equilibrium state. All equilibrium points constitute a binodal curve  
 31 (labeled as demixing curve in **Figure 1b**) that segment the single-phase regime from  
 32 the two-phase regime in a  $T$ - $\Phi$  plot. When the state transition of a hydrogel is reversible  
 33 only if such transition evolves along this binodal curve. Otherwise, this state transition  
 34 can be route-dependent and irreversible. Furthermore, the emergence of turbidity along  
 35 the phase separation depth is the macroscopic expression of light scattering at the  
 36 interface of biphasic interface when the size of polymer-rich phase is comparable to the  
 37 wavelength of visible light. This critical size can correspond to a composition point  
 38 ( $\Phi_t$ ). When the fraction of polymer-rich phase exceeds  $\Phi_t$  ( $\Phi_2 < \Phi_t$ ), the gel turns turbid.  
 39

1 Based on this general argument, the LCST behavior of a gel can be characteristic of  
2 reversible transparency-to-opacity transfer when three prerequisites are met: (1) it  
3 should be transparent at low-temperature state; (2) the initial state should be in  
4 (quasi)equilibrium state; (3) the composition point at high-temperature state should  
5 exceeds critical points of turbidity.

6 Although we recently demonstrate some transparent versions of hydrophobically  
7 modified hydrogels,<sup>32</sup> but they rarely demonstrated reversible LCST phase transfer.  
8 Such rarity can be ascribed to the initial out-of-the equilibrium state due to the network-  
9 forming process. For example, to prepare hydrophobic association hydrogel, a typical  
10 process is to expose a homogeneous solution of non-water-soluble polymer to water  
11 vapor. In this process, polymer undergoes gelation through solvent-water exchange.  
12 Good solvent for polymer is displaced by water, which is a poor solvent and can  
13 plasticize the polymer and mediate network-forming phase separation. This is an  
14 nonequilibrium process as the phase separation process can be arrested in an  
15 intermediate state due to vitrification or gelation.<sup>35</sup> Therefore, the as-prepared  
16 hydrophobic association hydrogel is usually in an out-of-the equilibrium state, which  
17 prohibits the thermal reversibility, as elucidated by a phase diagram with upper  
18 miscibility gap (origin region) correlated to the Gibbs free energy for the mixing of a  
19 binary system. Heating increases the phase separation depth with further demixing of  
20 phases. The phase-separated structure formed after heating can be preserved even after  
21 its cooling due to the reduced Gibbs free energy (**Figure S1**).

22

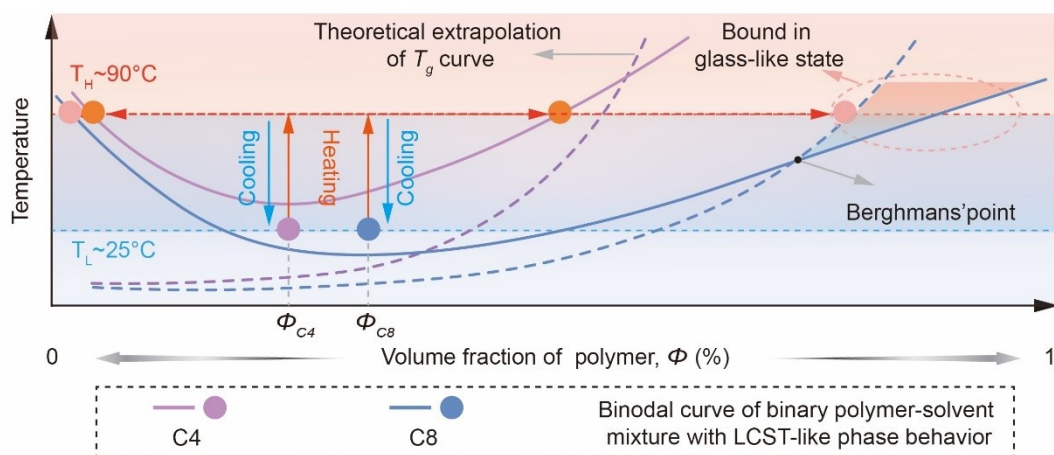
23

24

25

1 **Supplementary Note 3. Phase diagram of hydrophobically modified hydrogels**  
2 **and the kinetics of their LCST phase transfer.**

3 In addition of irreversibility, hydrophobically modified hydrogel (transparent version)  
4 could also suffer from sluggish switch between transparent and turbid state. This issue  
5 is originated from the formation of a vitrified-polymer-dense phase during LCST phase  
6 transfer. A representative feature for this system is the liquid–liquid demixing  
7 intercepted by the glass transition of the polymers at a so-called Berghmans' point  
8 (**Figure S2**).<sup>36</sup> Here, we further schematically illustrate the thermodynamic origins for  
9 this retarded coarsening effect from the relation between the binodal curve and the  
10 curve of glass transition temperature ( $T_g$ ) versus polymer volume fraction ( $\Phi$ ) in **Figure**  
11 **S2**. We reason that during the whole phase transfer process, the observed temperatures  
12 are much higher than the  $T_g$  of polymer-rich domain of FIRST systems, thus the  
13 mobility of chains is not significantly constrained, and the coarsening of phase  
14 separated domains can be quickly accomplished. This reasoning emphasizes the  
15 significance of PVB's high hydrophilicity in the FIRST hydrogel. Indeed, when we  
16 elongate the butyral side chains (C4) to octyl side chains (C8) in the initial polymer and  
17 maintain the acetalization degree of 30mol%, the thermally induced phase separation  
18 becomes completely irreversible (**Video S1**). The C8-length side chains exhibit greater  
19 hydrophobicity, leading to the formation of glass-like domains due to their relatively  
20 stronger interactions at application-related temperatures. By contrast, in concomitant  
21 with the phase separation process,  $T_g$  of polymer-rich domain of C8-based systems  
22 increase more rapidly than the binodal curve with the polymer volume fraction, thus,  
23 the observed temperatures can be below the  $T_g$  of polymer-rich domain of C8-base  
24 system. Thus, the phase separation will be kinetically arrested prior to complete  
25 equilibrium, exhibiting very slow coarsening rate.



1

2 **Figure S2.** An illustrative  $T$  (temperature)- $\Phi$  (composition) phase diagram of solvent-  
 3 polymer demixing interferes with the curve of glass transition of the hydrogels. The  
 4 purple (—) and blue (—) solid curve are the binodal curves for C4 and C8 based  
 5 hydrophobically modified hydrogels, respectively. The purple and blue broken lines are  
 6 the theoretical extrapolation of the glass transition lines for C4 and C8 based  
 7 hydrophobically modified hydrogels, respectively. The cross over point of the two  
 8 curves is the Berghmans' point. The initial state of C4 and C8-based hydrogel is in  $(T_L,$   
 9  $\Phi_{C4})$  and  $(T_L, \Phi_{C8})$  as indicated by  $\bullet$  and  $\bullet$ , respectively. Since the C4 is much more  
 10 hydrophilic than that of C8, therefore, the C4-based hydrophobically modified hydrogel  
 11 should have lower averaged volume fraction of polymer, with milder phase contrast. In  
 12 concomitant with the phase separation process, the  $T_g$  of polymer-rich domain also  
 13 increases. We have previously evidenced that the glass transition lines for C4-based  
 14 hydrogel should be always higher than that of C8-based hydrogel at the same  
 15 composition (*Macromolecules* 2021, 54, 13, 5962–5973). Thus, the observed  
 16 temperatures for phase separation can be much higher than the  $T_g$  of polymer-rich  
 17 domain of C4-based systems. The mobility of chains would not be significantly  
 18 constrained, and the phase separation can be rapidly completed to reach the spinodal  
 19 line (as indicated by  $\bullet$ ). By contrast,  $T_g$  of polymer-rich domain of C8-based systems  
 20 increase more rapidly than the spinodal curve with the polymer volume fraction, thus,  
 21 the observed temperatures can be below the  $T_g$  of polymer-rich domain of C8-base  
 22 system. Thus, the phase separation will be kinetically arrested prior to complete  
 23 equilibrium (as indicated by  $\bullet$ ), exhibiting very slow coarsening rate. This kinetically  
 24 arrested behavior empowers tunability on void-phase size.

25

26

27

28

29

30

31

1 **Supplementary Note 4. The appraisal standards for the FIRST features.**

2 Performance index is proposed to quantitatively compare the FIRST features among  
 3 different hydrogel systems. Indexes: 1: poor; 5: outstanding. The appraisal standards  
 4 from level 1 (poor/lowest) to level 5 (outstanding/highest) are detailed in **Tables S4-**  
 5 **S8. *It's crucial to highlight again that our evaluation is limited to hydrogels in a semi-***  
 6 ***solid state. Hydrogels in liquid or suspension states are not considered in this***  
 7 ***analysis, aligning with the specific focus of this manuscript.***

8 **Frost resistance:** Table S4 summarizes the freeze resistance scores of an array of  
 9 typical thermos-responsive hydrogels. Frost resistance refers to the antifreezing  
 10 performance of gel smart windows at minus zero degrees Celsius. Generally, gel smart  
 11 windows with water as dispersion medium are difficult to maintain high light  
 12 transmittance and mechanical properties in low temperature climate, which makes the  
 13 concept of multi-season general smart windows unable to be well implemented.

14 Unlike water, typical cryogenic protective agents, such as inorganic salts or polyols,  
 15 can effectively prevent the formation of overlarge ice-crystal by combining with ice  
 16 nucleating agents (anti-nucleating agents) and/or interacting with ice-like surfaces,  
 17 thereby further avoiding the loss of optical clarity and mechanical stretchability to a  
 18 large extent. For example, smart windows with water as the dispersion medium are  
 19 prone to freeze at low temperatures, leading to window cracking and whitening, which  
 20 seriously affects their large-scale application in real life. Therefore, if inorganic salt  
 21 solutions or polyols are used as dispersion media while retaining thermal responsive  
 22 properties, such gel smart windows will show advantages in multi-climate applications.

23 **Table S4.** Appraisal standards and scoring tables for the frost resistance of typical  
 24 LCST hydrogels that potential useful for thermochromic windows.

Hydrogel	Sample	Antifreezing (°C)	Score	Reference <sup>b</sup>
PNIPAm based hydrogel	PNIPAm	Na <sup>a</sup>	4	37
	P(NIPAm-co-DMAA)	Na <sup>a</sup>		
	PNIPA-PDMA	Na <sup>a</sup>		4
	PNIPAm/POSS hybrid	Na <sup>a</sup>		6
	PNIPAm/PEG	Na <sup>a</sup>		9
	PNIPAM/PEG/PANI	Na <sup>a</sup>		
	PNIPAm-GO composite	Na <sup>a</sup>		10
	PNIPAm-HPC composite	Na <sup>a</sup>		11
	Poly (N- isopropylacrylamide-co- acryloylaminozaobenzene	Na <sup>a</sup>		38

	PNIPAm/water/glycerol composite	-18 °C		39
	PNIPAm/ Ethyl alcohol composite	-20 °C		40
HPC based hydrogel	HPC-acrylamide	Na <sup>a</sup>	3	41
	HPC imbedded within PAM-PAA	Na <sup>a</sup>		42
	HPC/PAA	Na <sup>a</sup>		43
	HPC/water/glycerol composite	-10 °C		44
PNVCL (poly( <i>N</i> -vinyl caprolactam)) based hydrogel	PNVCL	Na <sup>a</sup>	1	45
	PNVCL-Clay composite	Na <sup>a</sup>		46
	PNVCL-titania composite	Na <sup>a</sup>		12
	H-ESO-HEC/poly(NVCL- <i>co</i> -DMAA)	Na <sup>a</sup>		15
POSS based hydrogel	PU/POSS	Na <sup>a</sup>	1	15
Other thermoresponsive hydrogel	(PTH)-PAAm	Na <sup>a</sup>		47
	PEG-ELP hybrid	Na <sup>a</sup>		48
FIRST	PVB/LiCl/water composite	-15 °C	4	This work

1 a. No available data was reported in relevant literature.

2 b. Please be aware that the cited references may not directly address the application of thermochromic  
3 windows. However, it is worth noting that the LCST hydrogels developed in these studies have the  
4 potential to serve as effective laminates for thermochromic windows.

5  
6  
7  
8  
9  
10  
11  
12  
13  
14  
15  
16  
17  
18  
19  
20

1

2 **Isochoric property:** For thermochromic windows, the LCST gels' dimensional  
 3 stability is a nontrivial issue. It is important to note that volume reduction is not unique  
 4 to LCST gels during the phase transition, as this transition invariably coincides with the  
 5 expulsion of liquid. Existing literature suggests potential strategies to mitigate volume  
 6 shrinkage, such as reducing enthalpy changes during phase transition or increasing the  
 7 polymer fraction,<sup>49</sup> although the effectiveness of these approaches needs to be  
 8 individually validated.

9

10 Ideally, hydrogels used in this context should exhibit inertness to temperature  
 11 variations, as any shrinkage would compromise their ability to shield light effectively.  
 12 The literature reports a wide range of phase separation-induced volume shrinkage for  
 13 LCST hydrogels, expressed as  $1-(V_{T>LCST}/V_0)$ , spanning from 1% to 90%. A qualitative  
 14 scoring system is applied, where systems with volume shrinkage below 10% are rated  
 15 as 5, those with shrinkage between 10% and 20% as 4, between 20% and 40% as 3,  
 16 between 40% and 60% as 2, and over 60% as 1.

17

18 **Table S5** summarizes the isochoric property scores of the thermo-responsive hydrogels  
 19 for thermochromic windows. We should emphasize again that we focus on hydrogels  
 20 in semi-solid state.

21 **Table S5.** Appraisal standards and scoring tables for the isochoric property of LCST  
 22 type hydrogels.

Hydrogel	Sample	Volume shrinkage (%)	Score	Ref <sup>a</sup>
PNIPAm based hydrogel	PNIPAm	Significant syneresis (present in Figure S3 in the cited paper)	1	3
	P(NIPAm-co-DMAA)	No significant syneresis	5	
	PNIPA-PDMA	No significant syneresis	5	4
	PNIPAm-PDMA	No significant syneresis	5	5
	PNIPAm/POSS hybrid	Significant syneresis (present in Figure 5 in the cited paper)	1	6
	PNIPAm/PEG	Significant syneresis (about 37%- as present in Figure 5 in the cited paper)	1	9
	PNIPAM/PEG/PANI	Significant syneresis (about 37-50% as present in Figure 5 in the cited paper)	2-3	
	PNIPAm-GO composite	Significant syneresis (about 40-65% as	1	10

		present in Figure 5 in the cited paper)		
	PNIPAm-HPC composite	No significant	5	11
	Poly ( <i>N</i> -isopropylacrylamide- <i>co</i> -acryloylaminozaobenzene,	Significant syneresis (about 94-96% as present in Figure 1 in the cited paper)	1	13
Average			~3	
HPC based hydrogel	HPC-acrylamide hydrogel	No significant syneresis	5	41
	PNIPAm-HPC composite	No Significant syneresis		11
	HPC imbedded within PAM-PAA	No Significant syneresis	5	17
Average			5	
	PNVCL	Significant syneresis (about 72% as present in Figure 7 in the cited paper)	1	16
PNVCL (poly( <i>N</i> -vinyl caprolactam)) based hydrogel	PNVCL-Clay composite	Significant syneresis (about 77%-83% as present in Figure 7 in the cited paper)	1	
	PNVCL-titania composite	Significant deswelling (no qualitative data for volume shrinkage is available, but data in Figure 3 in the cited paper demonstrate significant deswelling )	2	50
	H-ESO-HEC/poly(NVCL- <i>co</i> -DMAA)	Covalent crosslinking	1	12
Average			1.3	
POSS based hydrogel	PU/POSS	No significant shrinkage but obvious deformation upon heating (as present in Figure 2a in the cited paper)	5	15
Other thermoresponsive hydrogel	(PTH)-PAAm	No significant syneresis		47
	PEG-ELP hybrid	No significant syneresis		48
FIRST	PVB/LiCl/water composite	No significant shrinkage	5	This work

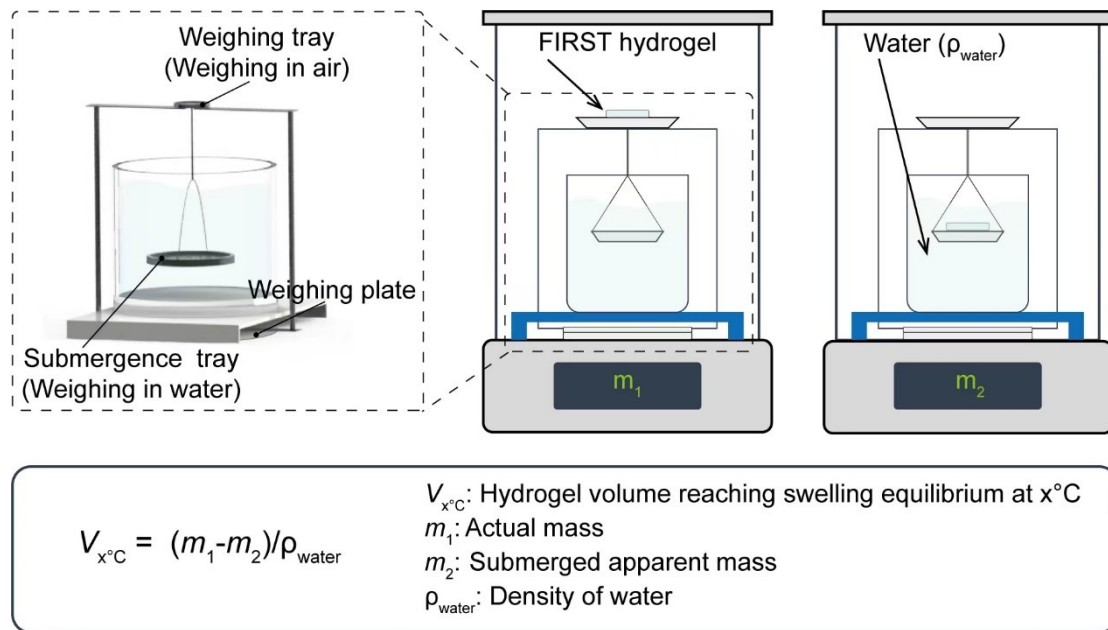
1 a. Please be aware that the cited references may not directly address the application of thermochromic  
2 windows. However, it is worth noting that the LCST hydrogels developed in these studies have the  
3 potential to serve as effective laminates for thermochromic windows.

4 **Hydrogel Volume Measurement Protocol for FIRST hydrogel:** The setup is  
5 schematically illustrated in **Figure S3**. Initially, a FIRST hydrogel was immersed in  
6 water at specific temperatures of  $x$  °C (e.g., 15 °C (below LCST) or 40 °C (above

1 LCST)) for a duration of about one hour. Subsequently, the sample was positioned on  
 2 a weighing tray in ambient air, and the mass was determined to be  $m_1$ . Continuing the  
 3 procedure, this sample was positioned on a submergence tray immersed in water at the  
 4 temperature of  $x$  °C. The mass was then measured and recorded as  $m_2$ . Obviously, the  
 5 value of  $(m_1 - m_2) \times g$  ( $g$  is gravitational acceleration constant) corresponds to the  
 6 buoyant force exerted. This buoyant force is equivalent to  $V_{x^\circ\text{C}} \times \rho_{\text{water}} \times g$ , where  $V_{x^\circ\text{C}}$   
 7 is the volume of FIRST hydrogel at temperature of  $x$  °C,  $\rho_{\text{water}}$  is the density of water.  
 8 Thus,  $V_{x^\circ\text{C}}$  of FIRST hydrogel at at temperature of  $x$  °C can be calculated using equation

9 as follows: 
$$V_{x^\circ\text{C}} = \frac{m_1 - m_2}{\rho_{\text{water}}}$$
 **Equation**

10 **S1**



11

12 **Figure S3.** Schematic Diagram and Principle of Buoyancy-Based Hydrogel Volume  
 13 Measurement Apparatus.

14 Accordingly, the volume shrinkage can be calculated by the following equation:

15 
$$\text{Volume shrinkage rate} = \frac{V_{x^\circ\text{C}} - V_{15^\circ\text{C}}}{V_{15^\circ\text{C}}}$$
 **Equation S2**

16 **Recyclability:** Considering the potential of massive consumption, recyclability of  
 17 laminates for thermochromic windows is significant to reduce the environmental  
 18 impact of the building industry and relieves the dependence on the fossil-fuel-based  
 19 raw materials.

20 For covalently crosslinked hydrogels, the permanent networks prevent recycling  
 21 because they cannot be dissolved by solvents or remolded by conventional processing  
 22 methods without degradation. Again, some polymer systems can be readily recycled  
 23 through so-called dynamic-covalent-bond mechanism. However, their realization  
 24 usually requires relatively harsh conditions, such high temperatures far above the

1 boiling point of water and/or the presence of hygroscopic catalysts. These conditions  
 2 can be incompatible with hydrated nature of hydrogels. We therefore score the  
 3 recyclability of this covalently crosslinked hydrogels as 0-1.

4 By contrast, most physically crosslinked hydrogels can be readily recycled at the end  
 5 of its lifespan through dissolution, processing, and post-crosslinking manipulation. For  
 6 example, the disposed FIRST hydrogel can be dried, redissolved in solvents and  
 7 remodeled into a freshly new sample. Thus, recyclability of these physically crosslinked  
 8 hydrogels generally ranks a high level. For some of them, recycling requires to be  
 9 conducted at elevated temperatures (e.g., PVA hydrogels), or multi-step related to the  
 10 destruction/reconstruction of the crosslinking knots (e.g., hydrogel crosslinked by metal  
 11 coordination bonds). After such multi-step process, it is difficult to ensure that the  
 12 recycled samples have identical components to that of fresh ones. In general, the  
 13 recyclability of physically crosslinked hydrogels is scored as 4-5.

14 **Table S6.** Appraisal standards and scoring tables for the recyclability of the  
 15 thermoresponsive hydrogels that potentially useful for thermochromic windows.

	Hydrogel	Crosslinking	Recyclability	Ref <sup>a</sup>
PNIPAM-based hydrogel	PNIPAM	Covalent crosslinking	1	3
	P(NIPAM- <i>co</i> -DMAA)	Covalent crosslinking	1	
	PNIPA-PDMA	Covalent crosslinking	1	4
	PNIPAM-PDMA	Covalent crosslinking	1	5
	PNIPAM/POSS hybrid	Covalent crosslinking	1	6
	PNIPAM/VO <sub>2</sub>	Covalent crosslinking	1	7
	PNIPAM/VO <sub>2</sub> @SiO <sub>2</sub>	Covalent crosslinking	1	8
	PNIPAM/PEG	Covalent crosslinking	1	9
	PNIPAM/PEG/PANI	Covalent crosslinking	1	
	PNIPAM-GO	Covalent crosslinking	1	10
	PNIPAM-HPC composite	Covalent crosslinking	1	11
	Poly (NIPAM - <i>co</i> -acryloylaminozaobenzene,	Covalent crosslinking	1	13
	Average		1	
PNVCL-based hydrogel	H-ESO-HEC/poly(NVCL- <i>co</i> -DMAA)	Covalent crosslinking	1	12
	PNVCL	Covalent crosslinking	1	16
	PNVCL-Clay composite	Physical	5 (However,	

		crosslinking (Clay surface)	the literature did not demonstrate the recyclability)	
Average			2.5	
HPC-based hydrogel	HPC imbedded within PAM-PAA	Covalent crosslinking	1	17
POSS	PU/POSS	Covalent crosslinking	1	15
Other thermoresponsive hydrogel	(PTH)-PAAm	Covalent crosslinking	/	47
	PEG-ELP hybrid	Covalent crosslinking		48
Others	EGP5/ATO	Covalent crosslinking	1	18

1 a. Please be aware that the cited references may not directly address the application of thermochromic  
2 windows. However, it is worth noting that the LCST hydrogels developed in these studies have the  
3 potential to serve as effective laminates for thermochromic windows.

4 **Scalability:** It's imperative to establish the capacity for large-scale production of the  
5 LCST polymer system, aligned with the demands of building-scale applications. This  
6 endeavour mandates a comprehensive evaluation of variables spanning chemical  
7 engineering, health, and market viability.

8 Scalability refers to the ability of a process to handle an increasing amount of work or  
9 demand. **Table S7** summarize the scalability scores of the thermo-responsive hydrogels  
10 for thermochromic windows. We mainly compare the industrial annual capacity,  
11 material preparation process, and whether it is conducive to large-scale preparation and  
12 commercialization. PNIPAm and PNVCL are typically synthesized by free radical  
13 polymerization of nonvolatile monomers. At least, two primary challenges should be  
14 addressed in achieving industrial scalability for these polymers. One challenge is the  
15 well-recognized occurrence of chain transfer reactions, which result in a low fraction  
16 of chemical covalent cross-links even without the presence of crosslinking agents-a  
17 phenomenon often referred to as the "self-cross-linking" effect.<sup>51, 52</sup> These difficulties  
18 in controlling crosslinking hinder the precise control of product quality on an industrial  
19 scale. Additionally, it is fundamental to acknowledge that the complete conversion of  
20 monomers in radical polymerization is inherently difficult to achieve. Residual  
21 monomers (e.g., NIPAM) and crosslinkers are notoriously challenging to eliminate,  
22 while these monomers can be toxic<sup>55</sup>, which raises health concerns, particularly in  
23 construction-related applications. Such issues become even more critical in the event  
24 of leakage. As a result, the score of scalability for these polymers is 1.

1 On the other hand, hydroxypropyl cellulose is synthesized through a more stable and  
 2 straightforward process involving the alkalization of cellulose, reaction with propylene  
 3 oxide, and neutralization with hydrochloric acid, followed by organic solvent  
 4 precipitation, washing, and drying, receiving a score of 3 for its production feasibility.  
 5 Meanwhile, POSS has a complex and lengthy synthesis process, making it unsuitable  
 6 for large-scale industrial production, earning it a score of 1. PVB, as a traditional bulk  
 7 chemical, can be synthesized economically through acetal reaction catalyzed by  
 8 inorganic acid in an aqueous phase, making it suitable for mass production.

9 **Table S7** Appraisal standards and scoring tables for the scalability of the thermo-  
 10 responsive hydrogels that potentially useful for thermochromic windows.

Hydrogel	Sample	Polymer raw materials annual industrial output (tons)	Raw materials preparation method	Preparation process	Score	Ref. <sup>a</sup>
PNIPAm based hydrogel	PNIPAM	Non-large-scale production	Free radical polymerization reaction	Monomer in situ polymerization	1-2	54, 55
	PNIPAM/VO <sub>2</sub>					7
	PNIPAM/VO <sub>2</sub> @SiO <sub>2</sub>					8
	P(NIPAm-co-DMAA)					37
	PNIPAm-HPC composite					11
HPC based hydrogel	HPC	Non-large-scale production	Etherification reaction	Gelling forming agent to promote gelation or Stir dispersion	3	56-59
	HPC/PAA			Stir dispersion		43
	PNIPAm-HPC composite			Monomer in situ polymerization		11
PNVCL based hydrogel	PNVCL	Non-large-scale production	Batch emulsion polymerization	Monomer in situ polymerization	1-2	60, 61

POSS based hydrogel	PU/POSS	Non-large-scale production	Complete hydrolysis method	Monomer in situ polymerization	1	15
Other thermoresponsive hydrogel	(PTH)-PAAm	Non-large-scale production	Free radical polymerization reaction	Monomer in situ polymerization		47
	PEG-ELP hybrid	Non-large-scale production	Free radical polymerization reaction	Monomer in situ polymerization		48
FIRST	PVB/LiCl/water composite	800,000	Acetal reaction	Non-solvent exchange	5	This work

1 a. Please be aware that the cited references may not directly address the application of thermochromic  
2 windows. However, it is worth noting that the LCST hydrogels developed in these studies have the  
3 potential to serve as effective laminates for thermochromic windows.

4

5

6

7 **Toughness:** The incorporation of tough mechanics offers additional benefits when  
8 considering thermochromic hydrogel as laminate for windows. These qualities enable  
9 the hydrogel to effectively resist crack propagation and potentially make it reusable, in  
10 situations where windows shatters.

11 Toughness is a measure of a hydrogel's ability to resist fracture or failure when  
12 subjected to an external force or stress. **Table S8** summarizes the toughness scores of  
13 the thermo-responsive hydrogels for thermochromic windows. It is often associated  
14 with the strength. Toughness can be estimated by measuring the fracture energy which  
15 is in the unit of joules per cubic meter ( $J/m^2$ ). The fracture energy of a material is  
16 determined by subjecting it to a controlled stress or load, and measuring the amount of  
17 energy absorbed by the material before it fractures or breaks. The higher the fracture  
18 energy of a material, the more energy it can absorb before failing, and the tougher it is  
19 considered to be. As shown in the above table, the fracture stress of FIRST hydrogel  
20 was 100 times higher than that of HPC hydrogel, and the elongation at break was nearly  
21 40 times that of PNIPAm hydrogel. This excellent mechanical property makes the  
22 FIRST hydrogel have a far-reaching application prospect in the field of intelligent  
23 response hydrogel. Although POSS-based hydrogels showed good elongation, the  
24 fracture stress was relatively small, so they got 4 points. Overall, the FIRST hydrogel  
25 gets 5 points on this board.

1 **Table S8.** Appraisal standards and scoring tables for the toughness of thermoresponsive  
 2 hydrogels that potentially useful for thermochromic windows.

Hydrogel	Sample	Fracture energy (kJ/m <sup>2</sup> )	Work of extension (kJ/m <sup>3</sup> )	Tensile strength (kPa)	Strain (mm/mm)	Score	Ref <sup>b</sup>
PNIPAM based hydrogel	PNIPAm	NA <sup>a</sup>	NA <sup>a</sup>	~ 4	~ 0.52		62
	PNIPAm-PDMA	~ 0.8	NA <sup>a</sup>	~ 70	~ 9	1~2	63
	PNIPAm-HPC composite	NA <sup>a</sup>	~ 120	~ 5.5	~3.6		11
HPC based hydrogel	HPC	NA <sup>a</sup>	NA <sup>a</sup>	NA <sup>a</sup>	NA <sup>a</sup>		64
	HPC/PAA	NA <sup>a</sup>	NA <sup>a</sup>	NA <sup>a</sup>	NA <sup>a</sup>	0~1	43
	PNIPAm-HPC composite	NA <sup>a</sup>	~ 120	~ 5.5	~3.6		11
PNVCL based hydrogel	PNVCL	NA <sup>a</sup>	NA <sup>a</sup>	NA <sup>a</sup>	NA <sup>a</sup>	1	60, 65, 66
POSS based hydrogel	PU/POSS	NA <sup>a</sup>	NA <sup>a</sup>	~ 20	~110	4	15
Other thermoresponsive hydrogel	PNIPA-PDMA (Side chain-PNIPA)	~ 0.03 (20 °C) ~ 0.32 (60 °C)	NA <sup>a</sup>	~ 4 (20 °C) ~ 20 (60 °C)	~ 2 (20 °C) ~ 3.3 (60 °C)		4
	PNIPA-PDMA (Side chain-PDMA)	~ 0.02 (20 °C) ~ 0.13 (60 °C)	NA <sup>a</sup>	~ 2 (20 °C) ~ 15 (60 °C)	~ 1.4 (20 °C) ~ 1.5 (60 °C)		
	PAAc/CaAc	NA <sup>a</sup>	149 (25 °C) 781 (70 °C)	~ 100 (25 °C) ~ 15000 (70 °C)	~ 6.5 (25 °C) ~ 0.7 (70 °C)		14
	(PTH)-PAAm	NA <sup>a</sup>	~300	~ 80	~ 8		47
	PEG-ELP hybrid	NA <sup>a</sup>	NA <sup>a</sup>	NA <sup>a</sup>	NA <sup>a</sup>		48
FIRST	PVB/LiCl/water composite	~ 70	12153	~ 1200	~ 21	5	This work

3 a. No available data was reported in relevant literature.

4 b. Please be aware that the cited references may not directly address the application of thermochromic  
 5 windows. However, it is worth noting that the LCST hydrogels developed in these studies have the  
 6 potential to serve as effective laminates for thermochromic windows.

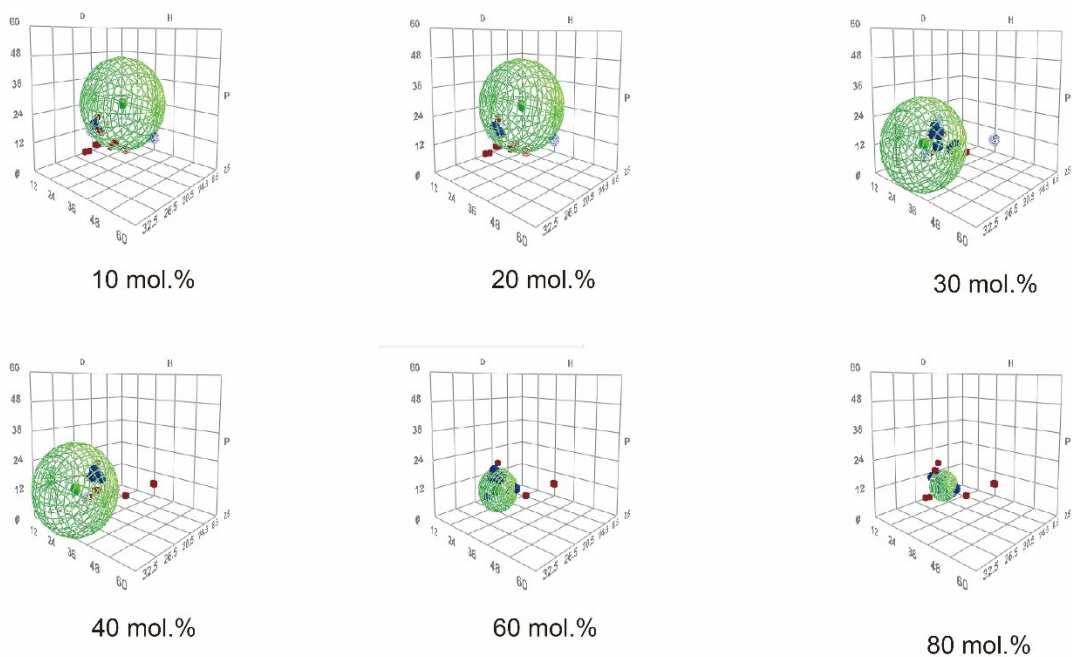
## Supplementary Note 5. Polymer solubility analysis.

1  
2 In this study, we utilized the solvent interaction test, also known as the solubility test,  
3 to investigate the interaction between different acetalization degrees of PVB samples  
4 and solvents. The results of these tests were further analyzed using the HSPiP software,  
5 developed by C. M. Hansen and widely used for determining the HSPs (Hansen  
6 Solubility Parameters). To characterize the solubility, the PVB samples were exposed  
7 to 30 different solvents. Each sample and the corresponding test solvent were combined  
8 in a sealed vial at a concentration of 100 mg/mL and maintained at 20 °C for 24 hours  
9 until equilibrium was reached. The interaction between the samples and solvents was  
10 evaluated using a method established by Hansen, which categorized the results as  
11 follows: 1 – Soluble, 2 – Almost soluble, 3 – Strongly swollen with slight solubility, 4  
12 – Swollen, 5 – Little swelling, 6 – No visible effect.<sup>65</sup> The solubility test results of the  
13 polymer samples in the 30 solvents were used directly as input data for the HSPiP  
14 software to calculate the HSPs values. A three-dimensional solubility sphere can be  
15 obtained by the HSPiP software. Its center represents the polymer, and its radius is  
16 defined as the radius of interaction ( $R_o$ ). The differences of HSPs between the various  
17 solvents and the polymer ( $R_a$ ) can be calculated by **Equation S3**,

$$18 \quad R_a = [4(\delta_d^s - \delta_d^p)^2 + (\delta_p^s - \delta_p^p)^2 + (\delta_h^s - \delta_h^p)^2] \quad \text{Equation S3}$$

19 where superscripts S and P indicate solvent and polymer, respectively. If  $R_a$  is smaller  
20 than  $R_o$ , it signifies that the solvent is likely to dissolve or strongly swell the polymer.  
21 Conversely, if  $R_a$  is equal to or greater than  $R_o$ , it suggests that the solvent is unable to  
22 dissolve the polymer or that there is little to no noticeable interaction between them.

23



1

2 **Figure S4.** Solubility spheres for the PVB samples with indicated molar content of  
 3 butyral content.

4

**Table S9.** The solubility tests results of PVB samples in 16 solvents.

<b>Molar content of Butyraldehyde groups (mol. %)</b>	10	20	30	40	60	80
Acetic anhydride	6	6	6	4	2	1
Acetone	6	6	5	4	2	1
Acetonitrile	4	4	4	5	6	6
Dimethyl Formamide	4	3	1	1	1	1
Dimethyl Sulfoxide	1	1	1	1	1	4
Ethanol	6	5	4	4	2	1
Ethyl Acetate	6	6	5	5	2	1
Isopropanol	6	6	5	4	2	1
Lactic Acid	6	6	6	6	5	3
N-Methyl-2-Pyrrolidone	1	1	1	1	1	1
Octane	6	6	6	6	6	6
1-Propanol	6	6	5	5	2	1
Tetrahydrofuran	6	6	5	5	3	1
Toluene	6	6	5	4	3	3
Water	1	2	3	5	6	6

5 1 – Soluble, 2 – Almost soluble, 3 – Strongly swollen with slight solubility, 4 – Swollen,

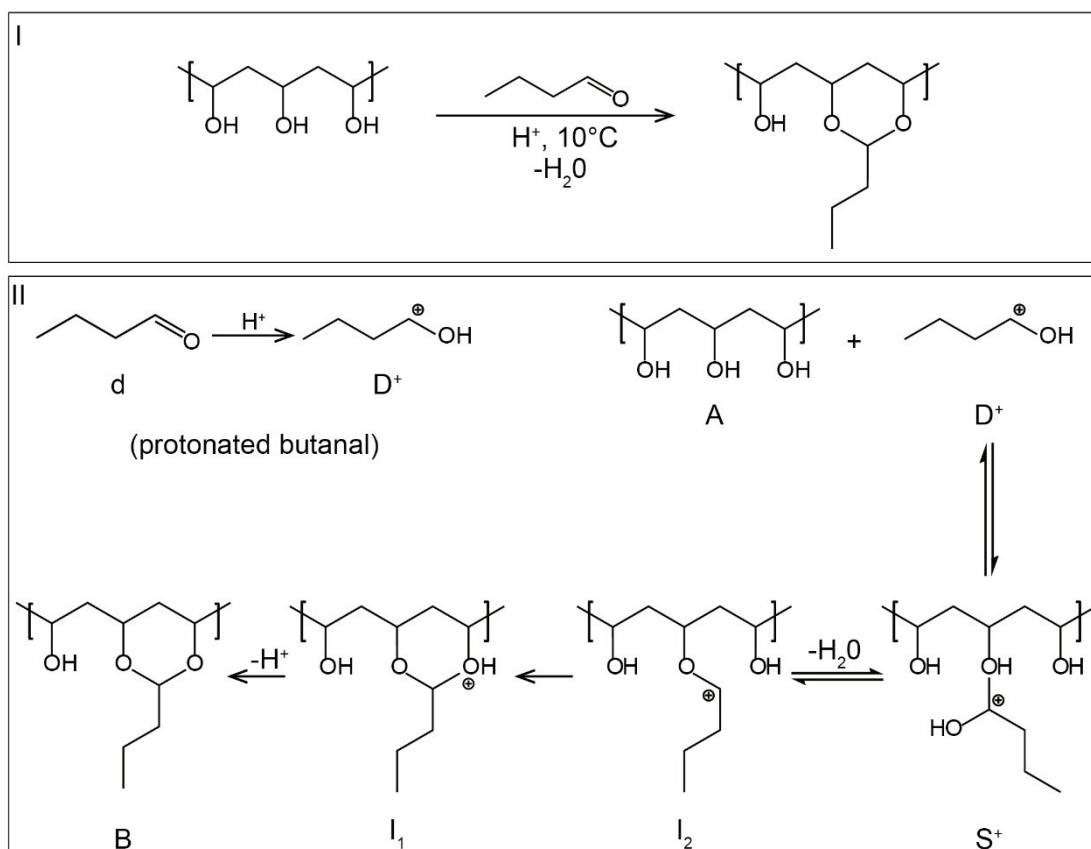
6 5 – Little swelling, 6 – No visible effect.

7

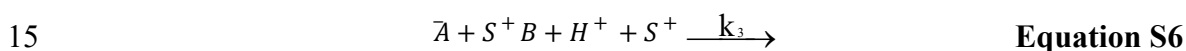
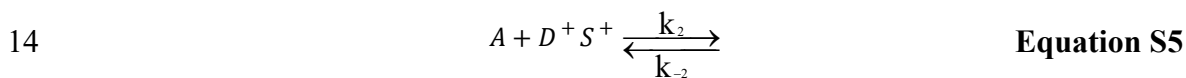
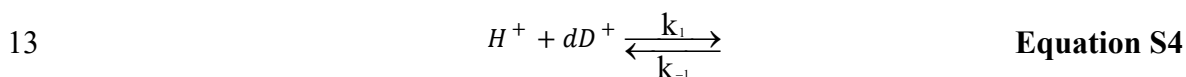
8

1 **Supplementary Note 6. Kinetics of polyvinyl butyral synthesis, and the molecular**  
 2 **structure and purity.**

3 **Scheme S1** illustrates the microscopic mechanism of acetalization kinetics in  
 4 homogeneous condition. The reaction between PVA and *n*-butanal can be simplified  
 5 into three steps: including the protonation reaction of *n*-butanal (**Equation S4**), the  
 6 hemiacetal generation reaction (**Equation S5**), and the acetal generation reaction  
 7 (**Equation S6**).



8  
 9 **Scheme S1. Reaction mechanism for PVB synthesis.** As indicated in **Scheme S1**, *d*  
 10 represents *n*-butanal, *D*<sup>+</sup> represents the protonated butanal, *A* represents single  
 11 hydroxyl group in the polymer, *S*<sup>+</sup> represents the hemiacetal group,  
 12 *B*<sup>+</sup> represents the charged acetal group, and *B* represents the acetal group.



1 Where  $\bar{A}$  specifically represent the neighboring hydroxyl groups to the hemiacetal.  
 2 Among these reactions, the protonation reaction (**Equation S4**) is usually considered  
 3 instantaneous, which means that the reaction equilibrium is established immediately.<sup>66</sup>  
 4 Here after,  $c_i$  is the concentration of certain species ( $i = A, d, D^+, S^+, B$ ), mol/L.  $K_1$  is  
 5 equilibrium constant of the first step reaction, L/mol.  $k_1$  is the rate constant for the first  
 6 step reaction, L/(mol•s).  $k_2$  is the rate constant for the second step reaction (hemi-acetal  
 7 generation), L/(mol•s).  $k_{-2}$  rate constant for the second reward step reaction (hemiacetal  
 8 degeneration),  $s^{-1}$ .  $k_3$  is rate constant for the third step reaction (acetal generation),  $s^{-1}$ .

9 Thus, the concentration ( $c$ ) of reactants in **Equation S5** follows the equation:

$$10 \quad c_{D^+} = K_1 c_{H^+} c_d \quad \text{Equation S7}$$

11 If a large amount of acidic catalyst is used in the experiment, the concentration of proton  
 12 ( $c_{H^+}$ ) can be considered constant and the concentration of  $D^+$  ( $c_{D^+}$ ) depends only on  
 13 the concentration of *n*-butanol ( $c_d$ ). For the acetal formation reaction (**Equation S6**),  
 14 we denote the hydroxyl group as  $\bar{A}$  to specifically denote the hydroxyl group adjacent  
 15 to the hemiacetal. Since only the adjacent hydroxyl groups can participate in the  
 16 reaction, and therefore, acetal formation is an intramolecular reaction. According to  
 17 Equation S7, the reaction rates of main components in this system can be described as:

$$18 \quad -\frac{dc_A}{dt} = k_2 K_1 c_{H^+} c_d - k_{-2} c_{S^+} + k_3 c_{S^+} \quad \text{Equation S8}$$

$$19 \quad -\frac{dc_d}{dt} = k_2 K_1 c_{H^+} c_d - k_{-2} c_{S^+} \quad \text{Equation S9}$$

$$20 \quad -\frac{dc_{S^+}}{dt} = -k_2 K_1 c_A c_{H^+} c_d + k_{-2} c_{S^+} + k_3 c_{S^+} \quad \text{Equation S10}$$

$$21 \quad -\frac{dc_B}{dt} = -k_3 c_{S^+} \quad \text{Equation S11}$$

22  
 23

1

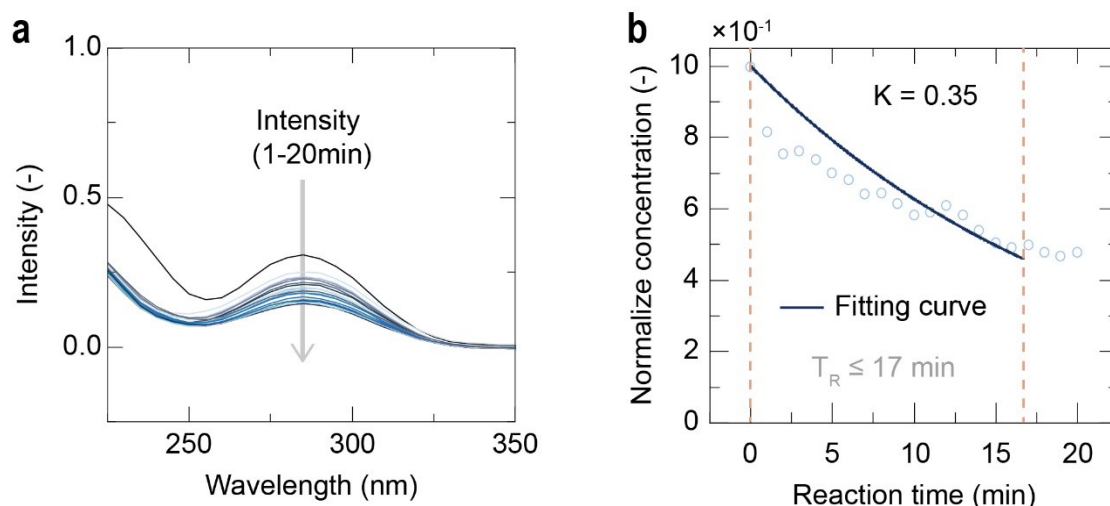
2 The hemiacetal group only reacts with one of neighboring hydroxyls, making the  
3 reaction rate independent of free hydroxyls in the solution. By appropriately controlling  
4 experimental conditions, including the relatively less amount of butyraldehyde (low  
5 acetylation degree) and very short reaction times (early stage of the reaction), it is  
6 reasonable to neglect the reverse reaction of **Equation S9**. Thus, the consumption of  
7 butyraldehyde can be estimated:

$$8 \quad -\frac{dc_d}{dt} \approx k_2 K_1 c_{A-0} c_d c_{H^+} \quad \text{Equation S12}$$

9 where  $c_{A,0}$  is the initial concentration of hydroxyl in reaction mixture. For more general  
10 situations where all of the component concentrations can be expressed as functions of  
11 time, the rate constants of  $k_{-2}$  and  $k_3$  can be fit using the above differential equations.

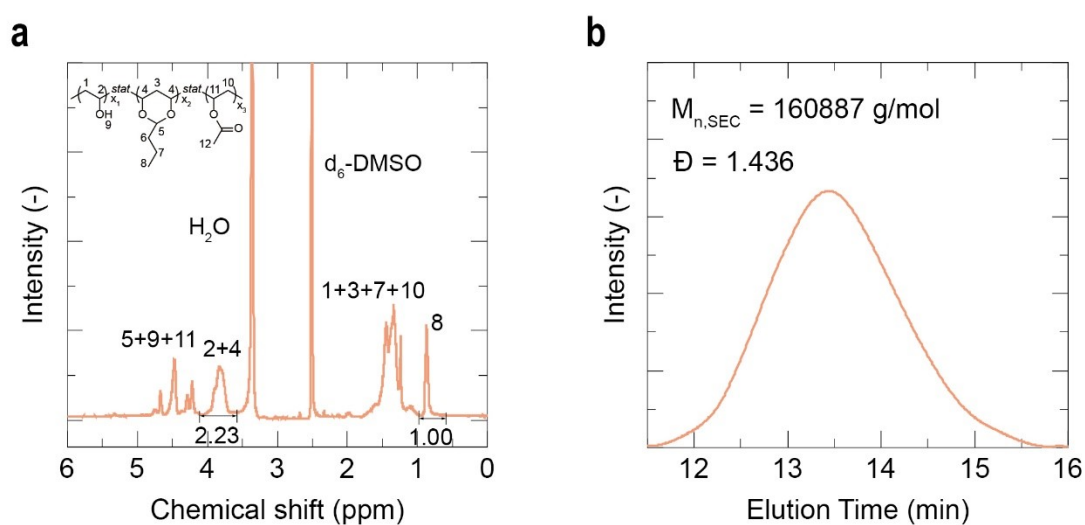
12 During the experiment, we purposely set  $c_{H^+} \gg c_d$  and  $c_{A-0} \gg c_d$ , so we can treat both  
13  $c_{H^+}$  and  $c_{A-0}$  as a constant during the reaction. So that we can determine the reaction  
14 rate constant by measuring the concentration changes of butyraldehyde.

15 To quantify the amount of residual butyraldehyde, we sample the reaction solution at  
16 different time intervals. After sampling, we adjust the pH of the reaction solutions to a  
17 value between 6.0 and 8.0 to stop the reaction immediately. Then, acetonitrile was  
18 immediately added to the solution to precipitate the PVA. Because low acetylation degree  
19 (less than 15%) PVB is a polar material, the product is then precipitated by adding 3-5  
20 times volume of acetonitrile to the stop reaction droplet. The product is then centrifuged  
21 at 1000 rpm using a differential centrifuge, and the supernatant is taken with a syringe  
22 and filtered using a filter membrane. The concentration of n-butanol in the mother  
23 liquid is measured using a UV-vis spectrophotometer (UV-3600 Plus, SHIMADZU)  
24 after solid centrifugation of PVB, and the change in butyraldehyde concentration is  
25 quantified by analyzing the characteristic absorption peak-peak intensity<sup>66</sup>. The UV-vis  
26 spectra are showcased in **Figure S5**.



1

2 **Figure S5. Demonstration of quasi-homogeneous reaction process for aqueous**  
 3 **phase synthesis of polyvinyl butyral.** a UV spectra for the solvent phase of the  
 4 reaction system. b The intensity of the reaction extracts taken out at different times in  
 5 the dynamic experiment under the UV-vis spectrophotometer (UV-3600 Plus,  
 6 SHIMADZU). Due to the high concentration of acid catalyst in the system, the  
 7 concentration of butyraldehyde decreased rapidly at the beginning and remained  
 8 basically unchanged after 17 minutes, indicating that the reaction entered dynamic  
 9 equilibrium at this time.



10

11 **Figure S6. Characterization of the product.** a Liquid  $^1\text{H}$  NMR spectrum of C4-0.3  
 12 (Solvent:  $d_6$ -DMSO). The DS (degree of substitution) can be defined as follows:

$$13 \quad \text{Molar content of PVB} = \frac{[\text{OH}]_s}{[\text{OH}]_0} \quad \text{Equation S13}$$

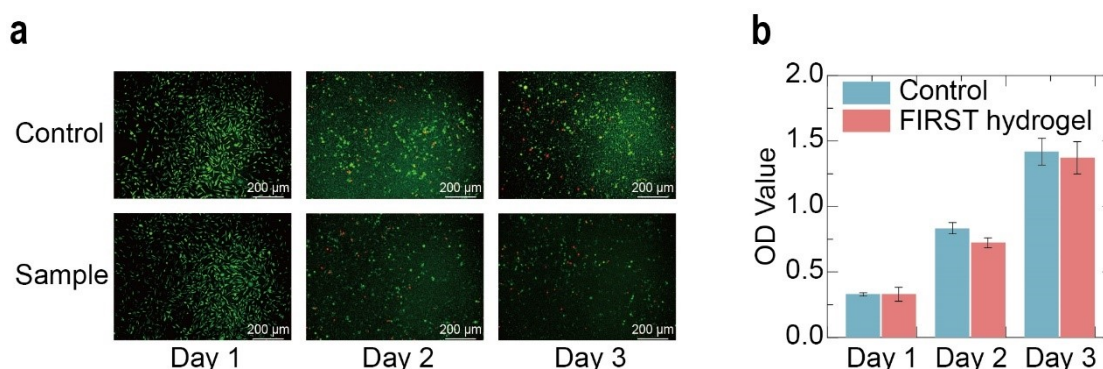
14 where  $[\text{OH}]_0$  is initial molar number of -OH groups on parent PVA;  $[\text{OH}]_s$  is substituted  
 15 molar number of -OH groups on C4-DS polymer. The  $[\text{OH}]_s/[\text{OH}]_0$  can be calculated  
 16 based on two peaks' areas of  $^1\text{H}$  NMR spectra:  $A_{12}$  and  $A_{2+4}$ . As shown in **Figure S6a**,  
 17  $A_{12}$  is the peaks' area of protons from the terminal  $-\text{CH}_3$  of alkyl side chain, thus the

1 substituted -OH groups on C4-DS can be calculated to be  $\frac{2}{3}A_{12}$ ; while  $A_{2+4}$  is the peaks'  
 2 area of protons from all -CH- segments on the PVA backbone, which is equal to that  
 3 of  $[OH]_0$ . Therefore,

$$4 \quad \text{Molar content of PVB} = \frac{2}{3} \times \frac{A_8}{A_{2+4}}$$

Equation S14

5 According to the integrated areas shown in **Figure S6a**, DS was calculated to be  
 6 approximately 0.30. **b** Gel permeation chromatography curve of PVB.



7  
 8 **Figure S7. In vitro cytocompatibility assessments of the FIRST hydrogel. a**  
 9 Representative bright-field and live-dead images of human embryonic lung cells (WI-  
 10 38) seeded on tissue culture plates in complete medium and FIRST hydrogel. This  
 11 shows that FIRST hydrogel is less cytotoxic to WI-38 and has good biocompatibility.  
 12 Scale bar = 200 μm. **b** MTT assay of cells cultured in complete medium and in FIRST  
 13 hydrogel leaching medium after 1, 2, and 3 days of seeding. In this cytotoxicity assay,  
 14 representative bright field and live-dead images of WI-38 that were seeded on tissue  
 15 culture plates in complete medium and the FIRST hydrogel. Calcein AM (0.5 μL/mL)  
 16 and PI (propidium iodide) (0.5 μL/mL) were diluted in DPBS to form the staining  
 17 solution, which was added to the well after removing the culture medium. Then, the  
 18 cells were incubated for 30 min at 37 °C in the dark. Live (green stain) and dead (red  
 19 stain) cells were imaged using an inverted fluorescence microscope (Observer 7, Zeiss,  
 20 Germany) on Days 1, 2 and 3 of culture. WI-38 was cultured in a 96-well tissue culture  
 21 plate (BD Biosciences) with 5000 cells/well. The leaching medium was prepared by  
 22 immersing the FIRST hydrogel in complete medium at 37 °C for 48 h. The proliferation  
 23 of WI-38 was quantitatively determined by MTT assays. The absorbance was measured  
 24 at 450 nm with a microplate reader on Days 1, 2 and 3 of culture.

25

26

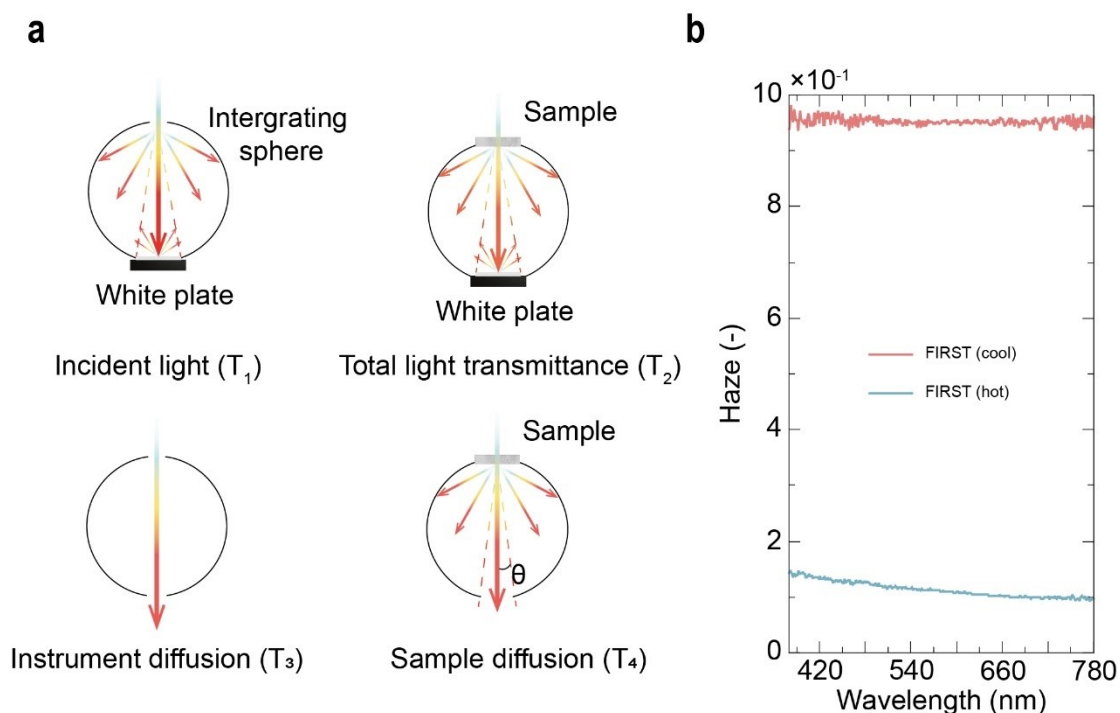
27

1

2 **Supplementary Note 7.A combination of multiple desirable**  
3 **properties.**

4 The design on molecular and condensed structure of PVB endow the FIRST hydrogel  
5 with a rare combination of multiple desirable properties, including rapid, reversible,  
6 and isochoric transparent-to-opaque transition, tough mechanics, high resilience and  
7 eco-friendly processability and recyclability.

8 Haze spectra of the hydrogels film under normal incidence irradiation from 250 to 800  
9 nm were monitored on the UV-vis-NIR spectrometer (Lambda 950, PerkinElmer,  
10 America) with an integrating sphere. The total light transmittance and sample diffusion  
11 of the sample is then measured and the haze value is calculated by the ratio of the two  
12 spectra (**Figure S8**).



13

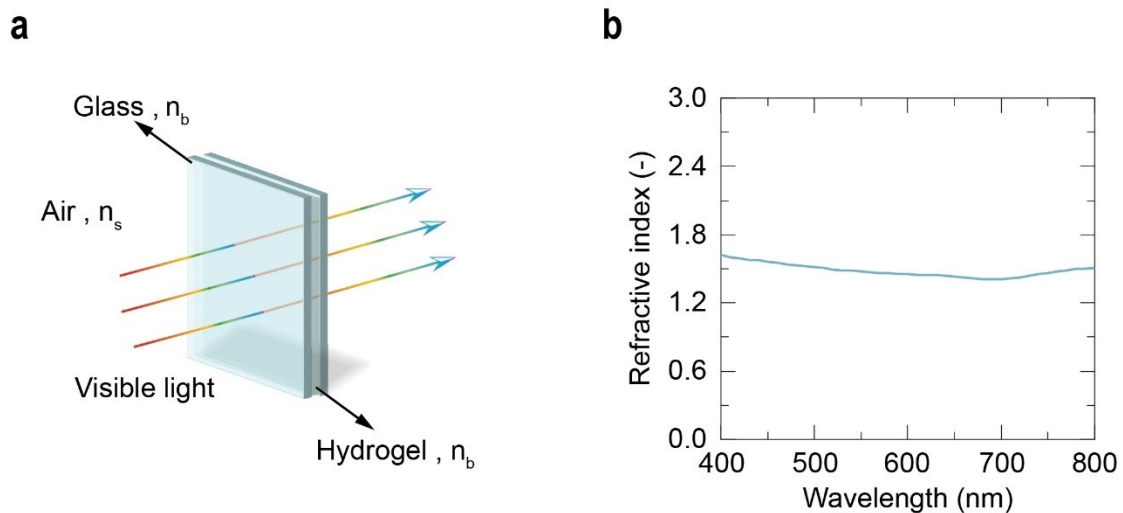
14 **Figure S8. Haze of FIRST hydrogel.** **a** Schematic diagram of hydrogel haze  
15 measurement device. **b** Haze spectra of FIRST hydrogels before and after phase  
16 transition. (The thickness of FIRST hydrogel was 300  $\mu\text{m}$ ).

17 As shown in **Figure S8**, decaying to 1.42 at 700 nm. To measure the haze with

1 spectrometer, we use an integrating sphere to illuminate the specimen diffusely; the  
 2 total port areas do not exceed 4.0% of the internal reflecting area of the sphere. The  
 3 specimen and light trap ports of the sphere is centered on the same great circle of the  
 4 sphere, and there is at least 2.97 rad (170°) of arc between their centers. The light exit  
 5 port subtends an angle of 0.14 rad (8°) at the center of the specimen port along the  
 6 viewing beam. Without specimen the axis of the viewing beam passes through the  
 7 centers of the specimen and light trap ports.

8 
$$Haze = \frac{T_d}{T_t} \times 100\% = \left( \frac{T_4}{T_2} - \frac{T_3}{T_1} \right) \times 100\% \quad \text{Equation S15}$$

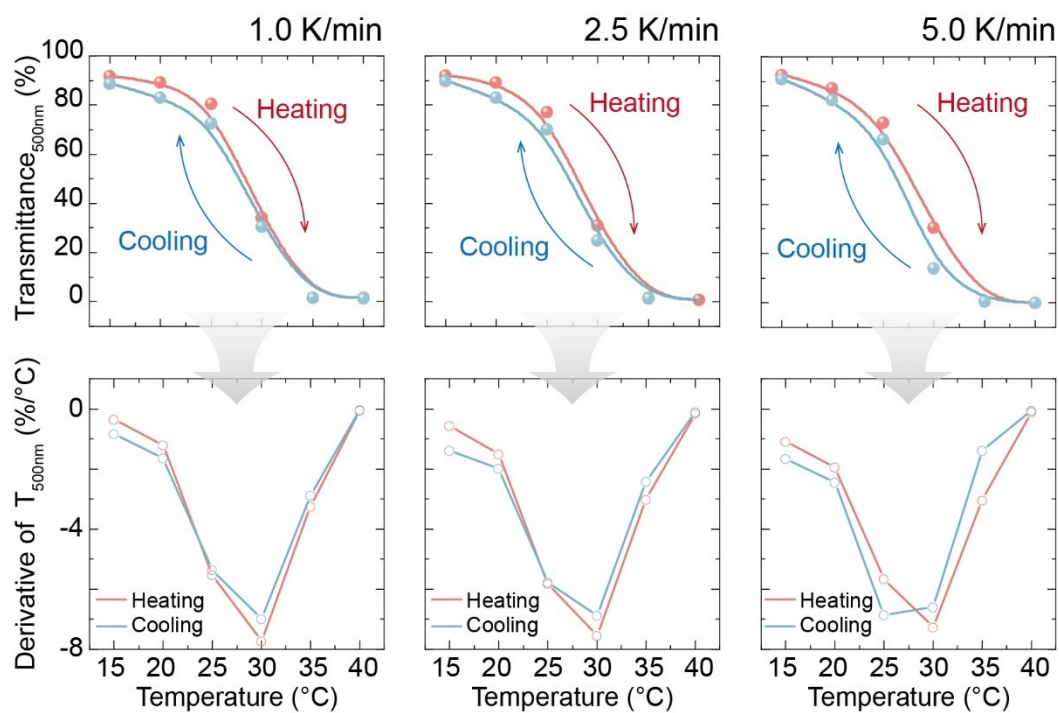
9 Wherein, incident light sample ( $T_1$ ), total transmittance ( $T_2$ ), light scattering rate of the  
 10 instrument itself ( $T_3$ ) and sample diffusion rate ( $T_4$ ) are obtained using an integrating  
 11 sphere. This method has been widely adopted in literatures<sup>[3,4]</sup> and recommended by  
 12 ASTM Committee.  
 13 ([https://www.academia.edu/30137927/Standard\\_Test\\_Method\\_for\\_Haze\\_and\\_Luminous\\_Transmittance\\_of\\_Transparent\\_Plastics\\_1](https://www.academia.edu/30137927/Standard_Test_Method_for_Haze_and_Luminous_Transmittance_of_Transparent_Plastics_1)).  
 14



15  
 16 **Figure S9. Refractive index determination of FIRST hydrogels. a** Refractive index  
 17 measurement scheme diagram. **b** Refractive index of FIRST hydrogels in the visible  
 18 wavelength band.

19

1



2

3 **Figure S10.** Hysteresis loop for the transmittance at 500 nm to show the LCST of  
4 FIRST hydrogel, and transmittance derivation curves for the FIRST hydrogel  
5 during the heating and cooling process.

6

7

8

9

10

11

12

13

14

15

16

1

2 The refractive index of our hydrogels was estimated based on the principle of light  
3 propagation on medium surface and polarization of light waves<sup>67</sup>. The setup for this  
4 measurement was schematically illustrated in **Figure S8**. In general, the test hydrogel  
5 was clamped between two species of glass slides with fixed thickness. Then, the light  
6 is incident vertically to the surface  $n_k$ ,  $n_b$  and  $n_s$  are the refractive index of air ( $\sim 1$ ), glass  
7 ( $\sim 1.5$ ) and hydrogel, respectively. According to the polarization character of light, when  
8 the light is incident vertically, Fresnel's formula can be simplified as

$$9 \quad t_s = t_p = \frac{2n_k}{n_k + n_b} \quad \text{Equation S16}$$

10 Wherein,  $t_s$  and  $t_p$  are the transmittance coefficient for  $s$  and  $p$  component,  
11 respectively. According to the propagation characteristics of light on media surface,  
12 the transmittance of air-glass interface and glass-hydrogel interface can be derived  
13 as :

$$14 \quad T_1 = \frac{n_b t_s^2}{n_k} = \frac{4n_k n_b}{(n_k + n_b)^2} \quad \text{Equation S17}$$

$$15 \quad T_2 = \frac{4n_b n_s}{(n_k + n_b)^2} \quad \text{Equation S18}$$

16 Wherein,  $T_1$  is the transmittance on the interface between air and glass, while  $T_2$  is  
17 the interface transmittance between glass and hydrogels. Based on the measurement  
18 structure designed by the experiment, when the transmitted light is detected by the  
19 light detector, it has passed through the four-layer media interface of air-glass, glass-  
20 gel, gel-glass, and glass-air, so the transmittance  $T$  output by the computer can be  
21 expressed as

$$22 \quad T_2 = T_1^2 T_2^2 \quad \text{Equation S19}$$

23 Combining Equations S17, S18 and S19, the refractive index can be derived to be

1

$$n_s = \left( 2 \sqrt{\frac{T_1(T_1 - \sqrt{T})}{T}} + \frac{2T_1\sqrt{T}}{T} - 1 \right) n_b$$

Equation S20

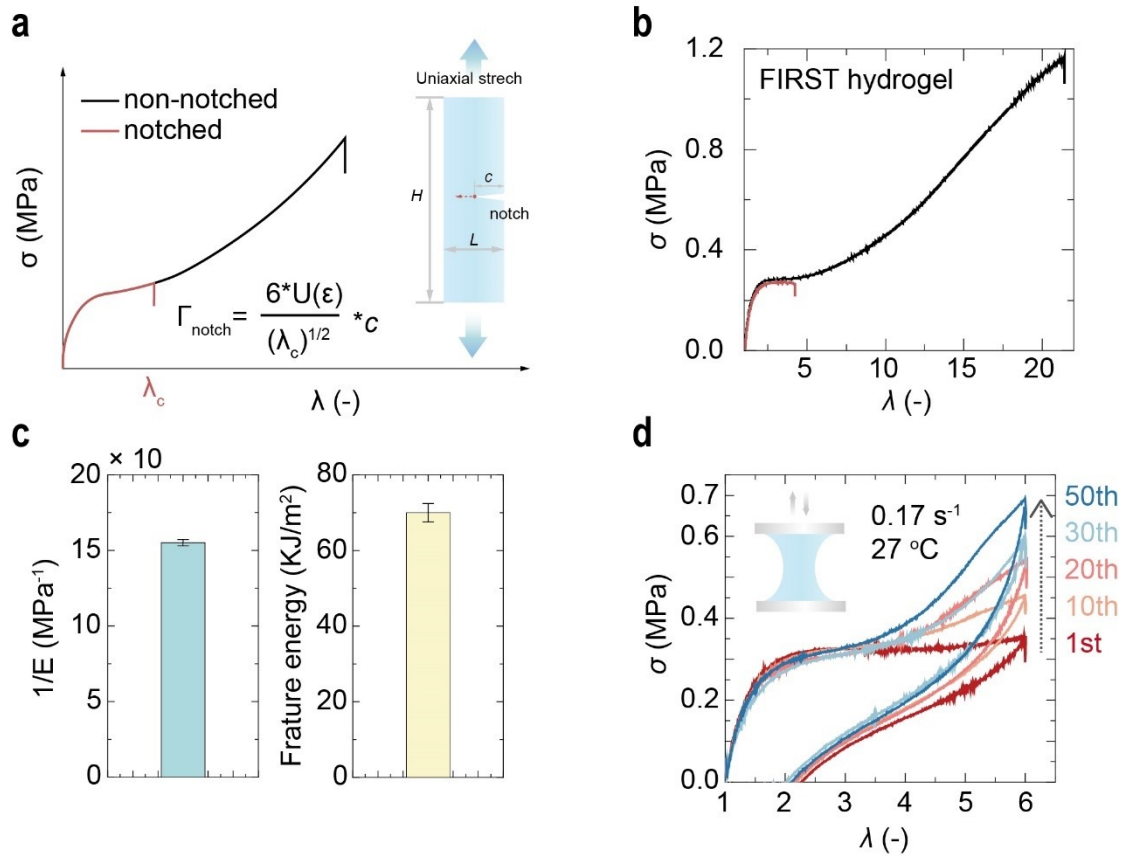
2 Under conditions with a constant air refractive rate  $n_k$  and glass refractive rate  $n_b$ , the  
 3 transmittance  $T_1$  at the gas-glass interface also remains constant at 96%, so **Equation**  
 4 **S20** can be simplified to the transmittance  $T$  output by the computer and the refractive  
 5 index  $n_s$  of the hydrogel relationship:

6

$$n = 0.96 \sqrt{\frac{5.76 - 6\sqrt{T}}{T}} + \frac{2.88\sqrt{T}}{T}$$

Equation S21

7 Where  $T$  is the transmittance as measured by using UV-vis-NIR spectrometer.



8

9 **Figure S11. Analysis of FIRST hydrogel tensile test images.** **a** Schematic diagram  
 10 of compliance and fracture energy calculation. **b** The stress( $\sigma$ )-stretch( $\lambda$ ) curves for  
 11 both single-edge notched and intact FIRST hydrogel, obtained by immersing the  
 12 hydrogel in 27 °C water at a stretch rate of 0.17 s $^{-1}$ . **c** Calculation of compliance (left)  
 13 and fracture energy (right) of FIRST hydrogel. **d** Mechanical dissipation of FIRST

1 hydrogels. Tensile tests were performed on a Zhuhai SANS (CMT2203) machine  
 2 equipped with a thermostatic water bath over a prescribed temperature at 27 °C. For  
 3 tensile tests, rectangular gels samples with a length of 20 mm, width of 8 mm and  
 4 thickness of 300 mm were used. The applied deformed rate was fixed at 0.17 s<sup>-1</sup> for  
 5 the tests. Three samples were measured for each construct to calculate the mean and  
 6 standard deviation. The nominal tensile stress( $\sigma$ ), nominal tensile strain( $\gamma$ ), elastic  
 7 modulus( $E$ ) were obtained from the stress-strain curves. The  $\sigma$  was calculated by  
 8 dividing the force ( $F$ ) by the cross-sectional area, and the  $\epsilon$  was obtained by dividing  
 9 stretched length by the original length. The elastic modulus was calculated from the  
 10 slope over 1%-5% elongation in the stress-strain curves. The work of extension ( $U$ )  
 11 was calculated by integrating the area of stress-strain curves.

$$12 \quad U(\epsilon) = \int_0^{\gamma} \sigma d\gamma \quad \text{Equation S22}$$

13 where  $U(\gamma)$  is the work of extension at a strain of  $\gamma$  and  $\sigma$  is the nominal tensile stress.

14 Single edge notched testing is used to determine the fracture energy. Two identical  
 15 samples with a length of 20 mm and width of 8 mm were used for tensile testing. A  
 16 notch with a length of 2 mm along the width was introduced by a razor blade cutting  
 17 into one of these two samples, with  $A$  as the area of the cross section of the unnotched  
 18 sample and  $L_0$  as the initial distance between the clamps. A stress-stretch curve was  
 19 measured for both the notched sample and an unnotched sample with the same initial  
 20 dimensions. The fracture energy based on the single edge crack method is given by:

$$21 \quad \Gamma_{noth} = \frac{6U_0}{\sqrt{\lambda_c}} \quad \text{Equation S23}$$

22 where  $c$  is the length of the crack and  $\lambda_c$  is the stretch at which crack propagation  
 23 initiates.  $U_0$  is the strain energy density, which is calculated by integration of the stress  
 24 versus engineering strain of unnotched samples.



1 **Supplementary Note 8. Chord Length Distribution Simulation Calculation.**

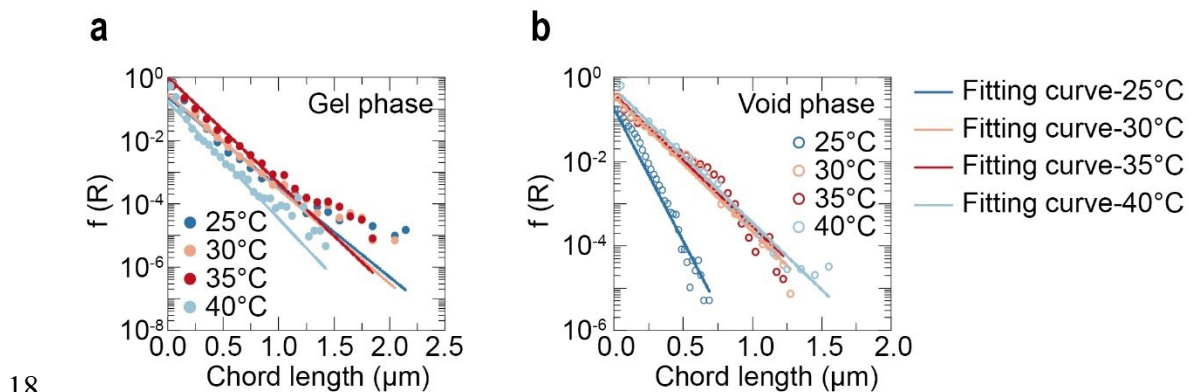
2 Each image of the stack is iteratively analyzed by a MATLAB® algorithm developed  
 3 by M. Ryan MacIver, which we repurposed to process the SEM images to obtain an  
 4 average chord length distribution representative of the entire image stack. Briefly, in  
 5 the selected stack, each 2D image was converted to grayscale, contrast enhanced, and  
 6 binarized. Then, a set of 10,000 randomly oriented lines was drawn on each image and  
 7 the number of segments defining the phase boundary (change from pore phase to gel  
 8 phase) was sorted according to the chord dimension  $R$  ( $\mu\text{m}$ ) to extract the frequency  
 9  $f(R)$  Histogram with bin size of 1  $\mu\text{m}$ . The minimum chord length in pixels is set to 2,  
 10 and the scale from pixels to metric units ( $\mu\text{m}$ ) is 0.002834.

11 All histograms show an exponential decay if plotted in a semi-log plot (*i.e.*  $\log f(R)$  vs  
 12  $R$  ( $\mu\text{m}$ )), that evolves according to:

13 
$$f_{\text{void-phase}} \propto \exp\left(\frac{-R}{\lambda_{\text{void-phase}}}\right) \quad \text{Equation S24}$$

14 
$$f_{\text{gel-phase}} \propto \exp\left(\frac{-R}{\lambda_{\text{gel-phase}}}\right) \quad \text{Equation S25}$$

15 where the persistence length  $\lambda$ , describes the characteristic length scales of the of the  
 16 two phases;  $\lambda$  was obtained for each gel by fitting the averaged exponential decays,  
 17 considering only the most frequent chord lengths.



19 **Figure S13. Chord-length analysis of FIRST hydrogel.** Chords are defined as the  
 20 segments that form when a set of randomly oriented lines cross phase boundaries.  
 21 The averaged frequency of chords with given length ( $f(R)$ ) for **a** gel phase and **b** void  
 22 phase. The lines are the fitting of the data to exponential decays. With the evolution  
 23 of phase separation, the chord length distribution and characteristic chord length of

1 the polymer phase decreased; on the contrary, the chord length distribution and  
2 characteristic chord length of the void phase increased.

### 3 **Supplementary Note 9. Small-angle Neutron scattering (SANS) analysis.**

4 SANS were performed at the China spallation neutron source (CSNS). Incident  
5 neutrons with wavelengths of 1–9 Å were selected using a double-disc bandwidth  
6 chopper, which was collimated to the sample by a pair of apertures. In the experiments,  
7 a sample to detector distance of 4 m and sample aperture of 6 mm were used. A 1 m  
8 square detector array was used composed of 120 linear <sup>3</sup>He gas tubes with a diameter  
9 of 8 mm, corresponding collimation lengths covering the scattering vector ( $q$ ) range  
10 between 0.005 and 0.1 Å<sup>-1</sup>. The scattering vector is given by  $q = \left(\frac{4\pi}{\lambda}\right)\sin\left(\frac{\theta}{2}\right)$ , where  $\theta$   
11 is the scattering angle. For each sample, the presented data were collected over ~120  
12 min at 100 kW. Neutron data are corrected for background scattering (empty sample  
13 holder), transmission and detector efficiency, and set to absolute units. The scattering  
14 was calibrated for absolute intensity using a 1.14 mm thick Bates-Poly62.5k standard.  
15 All samples were prepared in Hellma quartz cells with a 1 mm path length, and the  
16 measurements took place at 15 °C, 20 °C, 25 °C, 30 °C and 35 °C. The quartz cells  
17 were properly sealed to prevent any evaporation during the measurement.

18 Before SANS measurements, water in FIRST hydrogels was exchanged by D<sub>2</sub>O water  
19 by swelling specimen cut from hydrogels in excessive amount of heavy water. After  
20 24 h of swelling, the used heavy water was replaced by fresh one. The procedure was  
21 repeated three times.

22 For the SANS measurements, the hydrogel samples were equilibrated in SANS sample  
23 holders for 2 h at a starting temperature 15 °C. After the SANS data collection, the  
24 samples were heated up to a next temperature (20 °C) and allowed to equilibrate again  
25 for 2 h. Measurements at subsequent temperatures (25 °C, 30 °C, 35 °C) were carried  
26 out in the same way. The cooling cycle was further performed to affirm the  
27 reversibility. The scattering intensities at all temperatures were radially averaged and  
28 corrected for the sample transmission, room background, and detector efficiency using  
29 standard procedures.

30 Representative SANS patterns obtained for gels typically lack peaks corresponding to

1 strong correlations between strands or junctions due to the lack of long-range order<sup>68</sup>.  
 2 The behavior of scattering curves shows two features: a significant upturn at  $q < 0.02$   
 3  $\text{\AA}^{-1}$  and smooth decrease at  $0.02 \text{\AA}^{-1} < q < 0.1 \text{\AA}^{-1}$ . The scattered intensity for large  $q$  and  
 4 small  $q$  regions obeys power law with  $I \sim q^m$  and  $I \sim q^n$ , respectively, where both  $m$  and  
 5  $n$  are negative exponent. In related works on gels, thermal and frozen-in concentration  
 6 fluctuations have been made responsible for the characteristic fractal exponent of  $m$   
 7 and  $n$ , respectively<sup>69</sup>. As the temperature increases from 15 °C to 35 °C,  $m$  decreases  
 8 from -2.9 to -3.8, indicating the formation of sharper interfaces between different  
 9 phase domains. In the meanwhile,  $n$  decrease from -0.5 to -1. This decrease shows a  
 10 tendency of segment between hydrophobic clusters to change from a stretched  
 11 conformation to excluded volume chain conformation.

12 More quantitative information can be resolved by fitting the SANS spectra to D2O  
 13 was chosen as solvent because its scattering length density ( $\rho_{D_2O} = 6.36 \times 10^{10} \text{cm}^{-2}$ )  
 14 strongly differs from that of PVA ( $\rho_{PVA} = 0.634 \times 10^{10} \text{cm}^{-2}$ ) and the alkane chain  
 15 aggregates ( $\rho_{SH} = 1.67 \times 10^9 \text{cm}^{-2}$ ) As confirmed in a previous study, the replacement of  
 16  $H_2O$  with  $D_2O$  does not induce significant modification of the transition temperature in  
 17 thermo-responsive polymers<sup>70</sup>. The SANS spectra were fitted by using Gauss-  
 18 Lorentz-gel model:

$$I(q) = A \frac{1}{\left(1 + \left(D + \frac{1}{3}\right)q^2\zeta^2\right)^{\frac{D}{2}}} + Be^{\left(-q^2\frac{R_g^2}{3}\right)} + I_{bg}$$

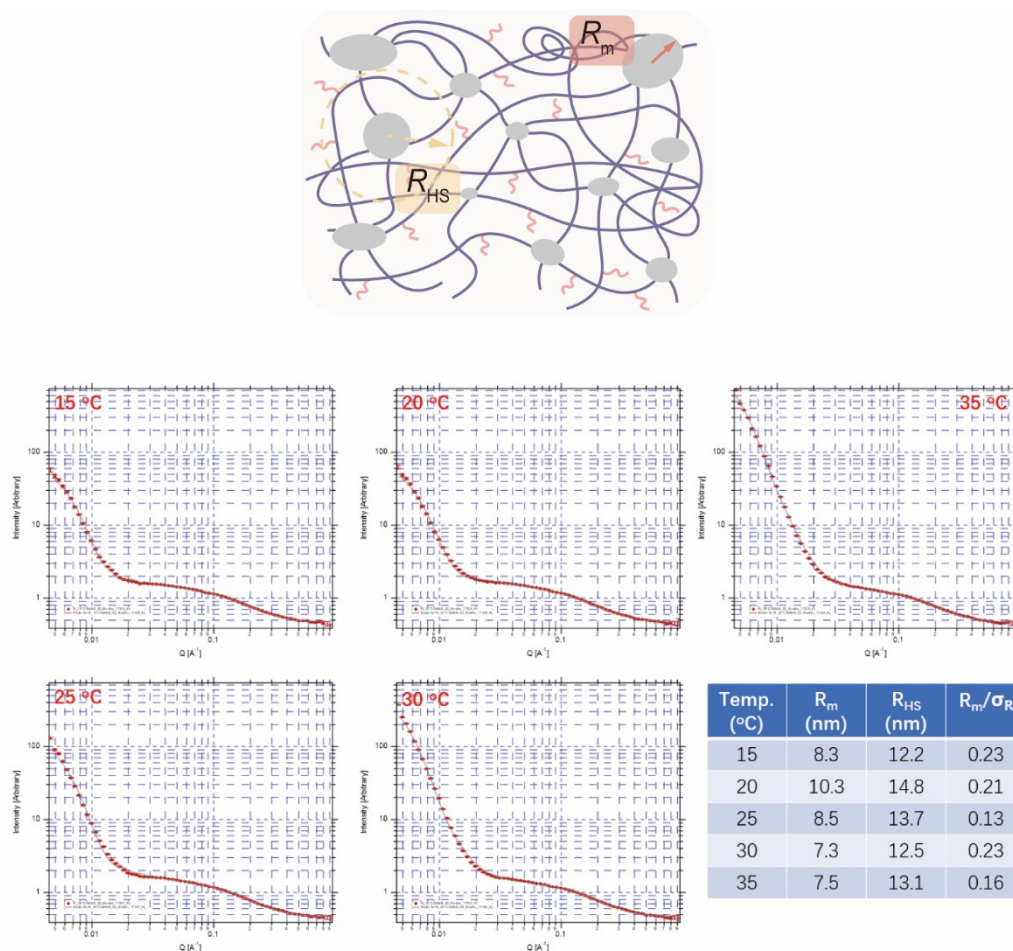
19

**Equation S26**

20 The A and B represents Lorentz and Guinier scaling factors, respectively. D is the  
 21 Porod exponent, giving an estimate of the roughness of the interfaces between  
 22 different domains of inhomogeneities. As summarized in **Figure 3b**, fitting results  
 23 shows that the correlation length  $\zeta$  decreases with temperatures, whilst the Porod  
 24 exponent and  $R_g$  increases from -0.5 to -1.0 and from 30 nm to 50 nm, respectively.  
 25 All these transitions showed an abrupt jump to a plateau value at around 28 °C.

26 To provide additional validation for the concept of nodules, we employed a hard-sphere  
 27 model to effectively analyze the SANS data (**Figure S14**). Within this model, the  
 28 nodule is represented by a repulsive hard sphere potential, defined by a mean radius

1 with a specific size distribution.



2

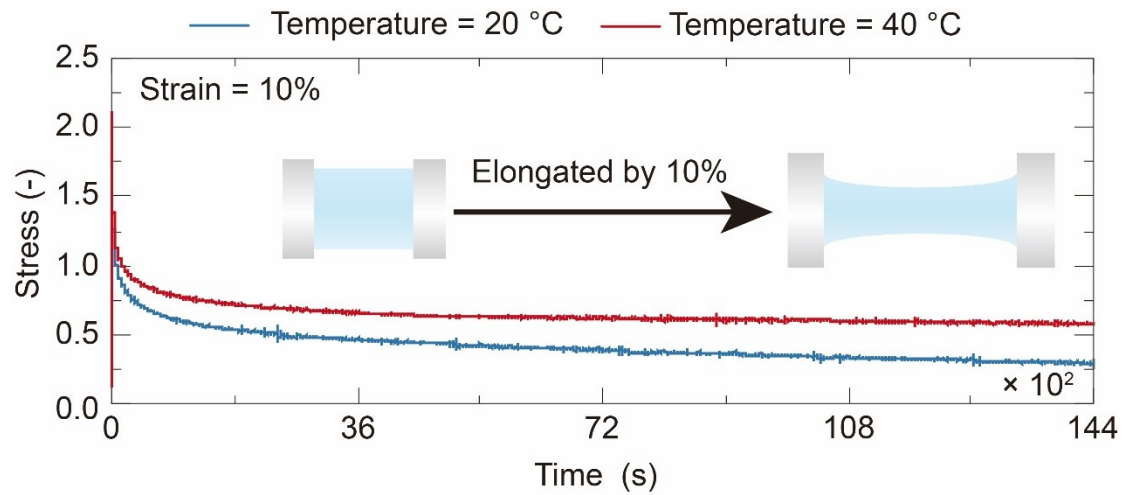
3 **Figure S14: Schematics for the characteristic structures resolved from the SANS**  
 4 **spectra by using hard-sphere model.** These structural parameters are summarized in  
 5 inset table; The concept of "nodules" can be understood as instances of structural  
 6 diversity occurring at the micro- or mesoscale. In particular, the butyl side chains have  
 7 the capability to self-organize into isolated spherical assemblies with short-range  
 8 correlations. These hydrophobic regions function as points of scattering for Small-  
 9 Angle Neutron Scattering (SANS), thereby reflecting the characteristic length in the  
 10 actual spatial arrangement. Such structure can be generally described by a hard-sphere  
 11 model. In this model, such nodules can be described as a repulsive hard sphere potential  
 12 of radius  $R_{HS}$  and a polydispersity that can be defined by  $\sigma_R/R_m$ , where  $R_m$  is the mean  
 13 radius of the distribution with standard deviation  $\sigma_R$ . The fitting results are summarized  
 14 in **Figure S14**. The data were analysed by using Igor software by using the Percus-  
 15 Yevick disordered hard-sphere model (<https://www.nist.gov/ncnr/data-reduction-analysis/sans-software>). This model has been reported to be sufficiently well related to  
 16 the structure of hydrophobic association hydrogels.  
 17

18

19

20

**Supplementary Note 10. Rheological characterization and tensile tests.**

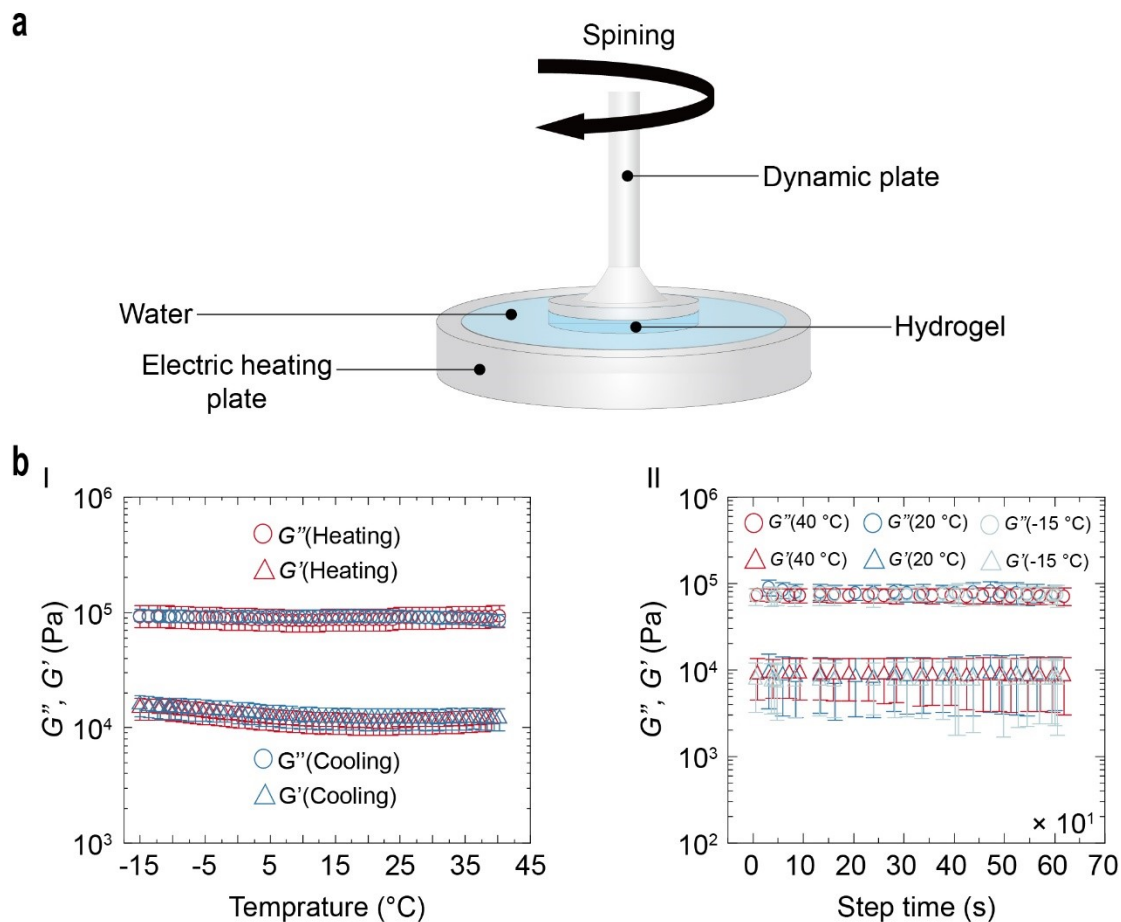


1

2 **Figure S15. Stress relaxation at tensile strain of 10% at temperature of 20°C and**  
 3 **40 °C.** Stress relaxation map of FIRST hydrogel before and after phase transition.  
 4 Clearly, significant residual stress can be observed even after over relaxation of 4 hours.  
 5 This result suggests the existence of permanent crosslinks. Counterintuitively, the residual  
 6 normalized stress at 40 °C is larger than that at 20 °C. One possible explanation is that  
 7 the retractive forces are partially of entropic origin. During this stress relaxation  
 8 experiment, we first apply a fixed amount of deformation, and then measure the load  
 9 required to maintain this specific deformation as a function of time.

10

11



1  
 2 **Figure S16. Rheological characterization of FIRST hydrogels.** **a** Schematic diagram  
 3 of rheological characterization. **b** Temperature-ramp rheological test (**b-I**) and  
 4 Oscillation rheological test (**b-II**) of FIRST hydrogel. As shown in **Figure S16b**, the  
 5 modulus of hydrogels almost did not change before and after the phase transition,  
 6 indicating that the phase transition components have no significant mechanical  
 7 contribution to FIRST hydrogels. Considering the dispersity of polyvinyl alcohol in  
 8 chemical modification process, it is assumed that the phase change component is mainly  
 9 composed of weakly hydrophobic parts. We guessed that this elastic network structure  
 10 may be formed by the strong hydrophobic part through topological entanglement  
 11 crosslinking.

12

13

14

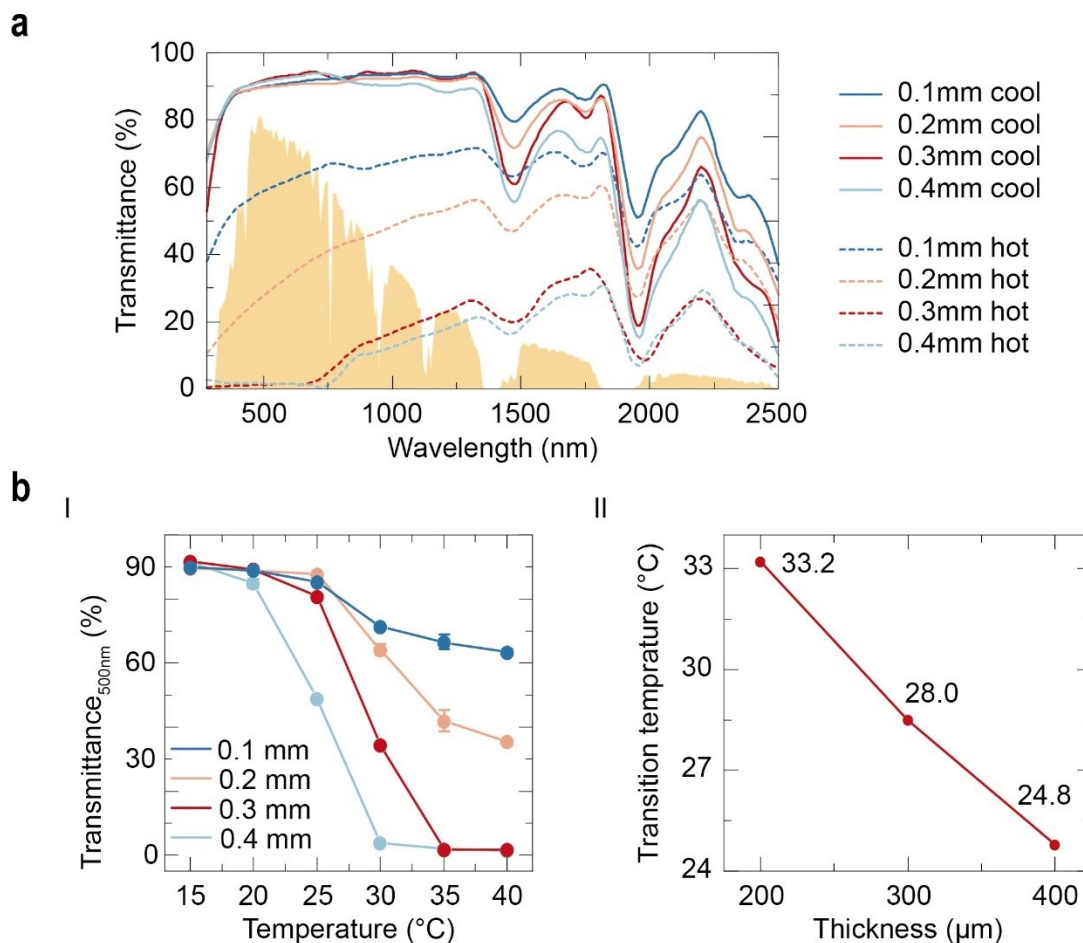
15

16

17

18

1 **Supplementary Note 11. Light and thermal regulation capabilities of FIRST**  
 2 **hydrogel laminated window.**



3

4 **Figure S17. Thickness dependence of the optical properties of FIRST hydrogels. a**  
 5 UV-vis-NIR spectra of FIRST hydrogels with thickness of 0.1mm, 0.2mm, 0.3mm, and  
 6 0.4mm. **b-I** Light transmittance of 0.1-0.4mm FIRST hydrogel at 500nm as a function  
 7 of temperature. If the corresponding temperature when the transmittance reaches 50%  
 8 is defined as the phase transition temperature, it can be found that the phase transition  
 9 temperature of FIRST hydrogel decreases with the increase of thickness. **b-II**  
 10 Dependence of phase transition points on FIRST thickness. The transmittance of 0.1  
 11 mm FIRST hydrogel could not decrease to 50% in this temperature range, and the phase  
 12 transition temperature could not be defined as described above. As shown in the **Figure**  
 13 **S17** with the increase of thickness, the shielding effect of FIRST hydrogel after phase  
 14 transformation on NIR spectrum is enhanced. Combined with the discussion results,  
 15 0.3mm FIRST hydrogel was finally selected as the object for further discussion and  
 16 testing. Transmittance and reflectance spectra were collected on a UV-vis-NIR  
 17 spectrophotometer system with an integrating sphere (UV-3600 Plus, SHIMADZU,  
 18 Japan). The spectrophotometer was connected to a constant temperature ice bath for  
 19 heating and cooling.

1 The  $T_{lum}$ ,  $T_{IR}$ , and solar transmittance  $T_{sol}$ , were calculated:

$$T_{lum/IR/sol} = \frac{\int \phi_{lum/IR/sol} T(\lambda) d\lambda}{\int \phi_{lum/IR/sol} d\lambda} \quad \text{Equation S27}$$

2

3

$$\Delta T_{lum/IR/sol} = T_{lum/IR/sol}^{40^\circ\text{C}} - T_{lum/IR/sol}^{15^\circ\text{C}} \quad \text{Equation S28}$$

4 Long-wavelength infrared light reflectance spectroscopy in the wavelength range (2.5  
5 to 16  $\mu\text{m}$ ) were measured by a Fourier transform infrared spectrometer (Nicolet 6700,  
6 Thermo Fisher, America) and a gold-plated integrating sphere, with an external sample  
7 temperature change table and a ramp rate of 1 K/min. Without considering absorption,  
8 the emissivity is calculated by the following equation:

9

$$\varepsilon = 1 - R \quad \text{Equation S29}$$

$$\bar{\varepsilon}_{LWIR} = \frac{\int I_{BB}(T, \lambda) \varepsilon(T, \lambda) d\lambda}{\int I_{BB}(T, \lambda) d\lambda}$$

10

Equation S30

11 Here  $I_{BB}(T, \lambda)$  is the spectral intensity emitted by a blackbody and  $\varepsilon(T, \lambda)$  is the surface's  
12 angular spectral thermal emittance in the range of 8–13  $\mu\text{m}$ .

13 **Indoor Thermal Test Procedure.** The indoor thermal test is a proof-of-concept for the  
14 FIRST hydrogel, which can both regulate solar energy and store thermal energy. This  
15 test provides a controlled environment without temperature fluctuations for the  
16 experiment and compares 4 samples: glass panel, Low-E glass, FIRST hydrogel and  
17 laminated glass. With this test, it can accurately assess the effectiveness of the FIRST  
18 hydrogel. The ambient temperature of the indoor lighting test is 25 °C. The indoor test  
19 glass box is made of one plexiglass box, five 2 cm thick Styrofoam pieces with black  
20 inside and different samples. Thermocouples are used to detect the temperature of 2  
21 different parts in the glass box: the inner surface of the window (temperature sensor A)  
22 and the air temperature in the geometric center of the box (temperature sensor B).  
23 For the 1000 W power solar lamp used in the experiment, the area between the lamp  
24 and the glass box related to aluminum foil to prevent heat loss. After turning off the  
25 solar light, the unit cools down naturally.

1 **Outdoor Thermal Test Procedure.** The outdoor test was designed to compare the  
2 energy-saving performance of glass panel, Low-E glass, 0.3mm-thick DI water, and  
3 FIRST hydrogel samples. It provides a realistic experiment environment with  
4 temperature fluctuation. A box (inner dimension: 15 cm × 15 cm × 20 cm) with glass  
5 panel (glass thickness is 5 mm, dimension: 20 cm × 20 cm) on the top was set as a  
6 control sample with thermocouple sensors in the geometrical center. The rest of testing  
7 setup has the same design as the control sample, while the glass panel was replaced by  
8 glass panel, Low-E glass, 0.3mm-thick DI water, and FIRST hydrogel, respectively.  
9 For the outdoor demonstration in hot temperature, the four setups were placed outdoor  
10 without any shelter and subjected to direct sunlight. The data were recorded every 10  
11 min in Guangzhou.

12

13

14

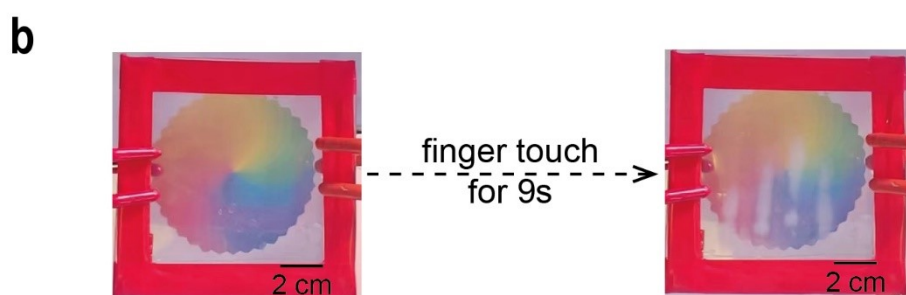
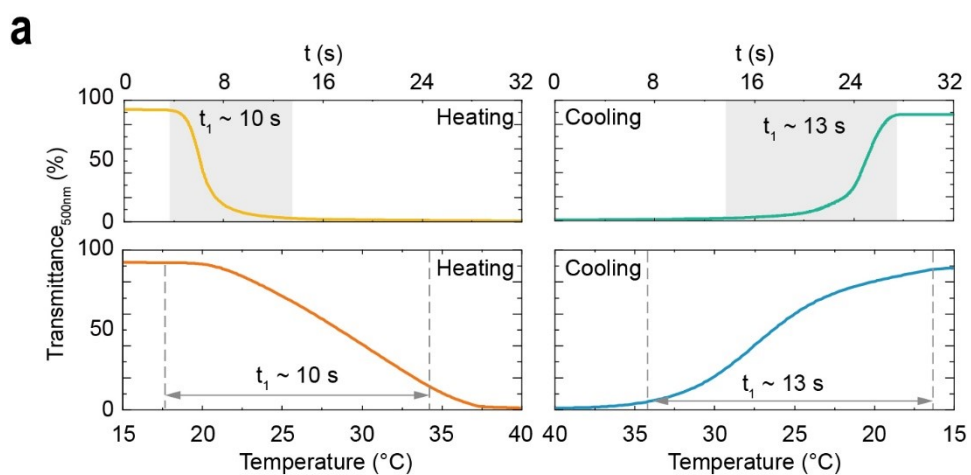
15

16

17

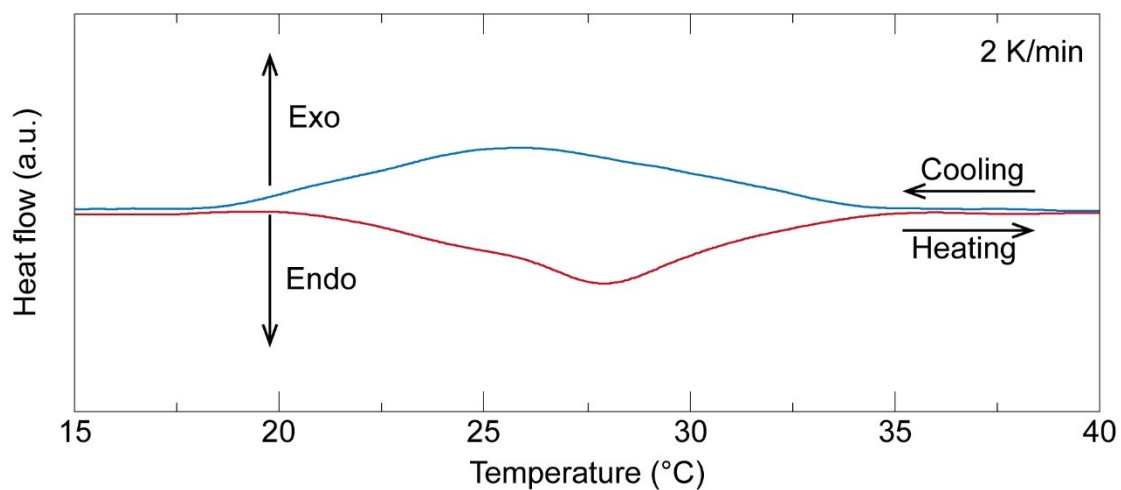
18

19



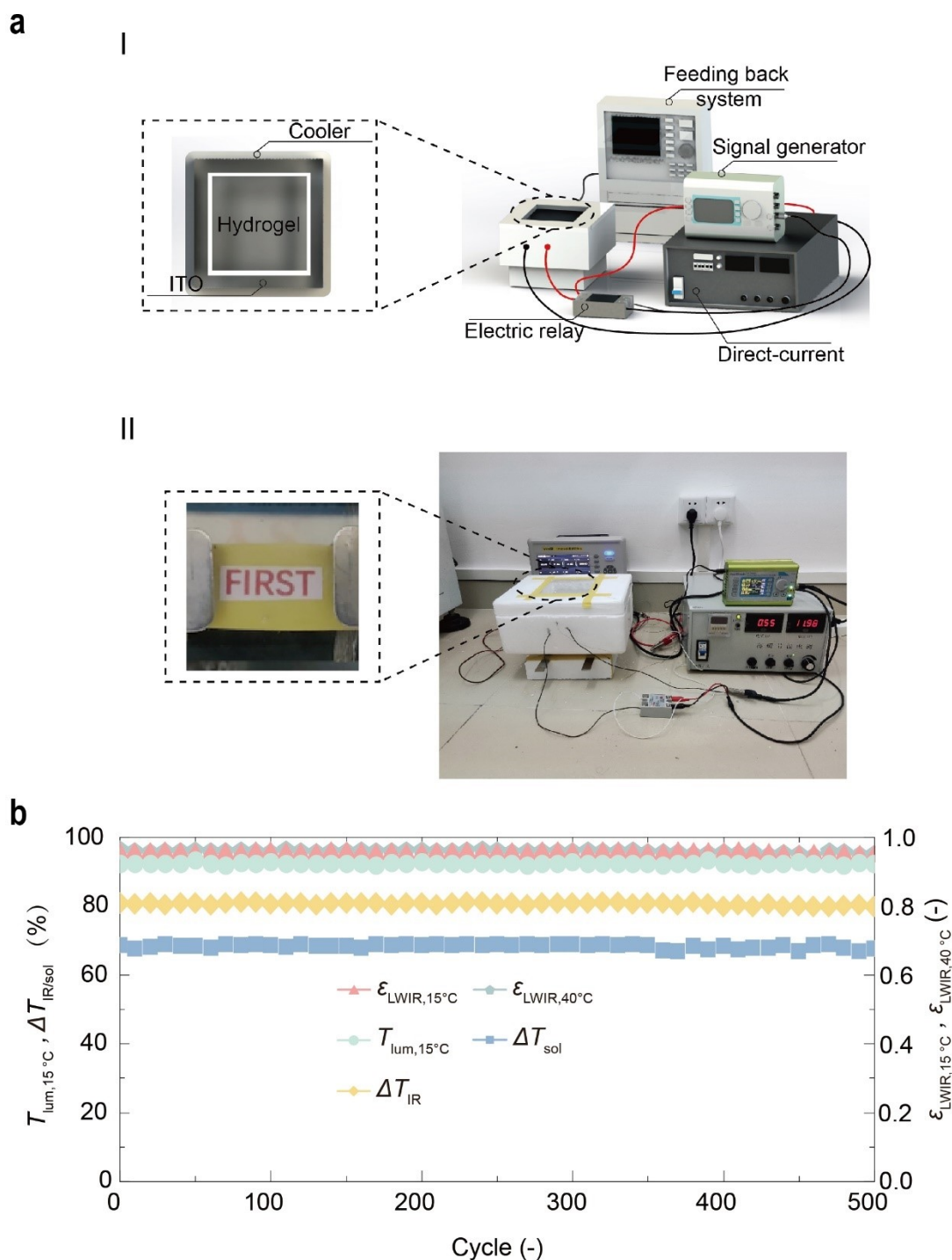
1

2 **Figure S18.** The thermal response curves of the FRIST hydrogels and the phase  
3 transition photographs (see **Video S3**) triggered by finger touch.



4

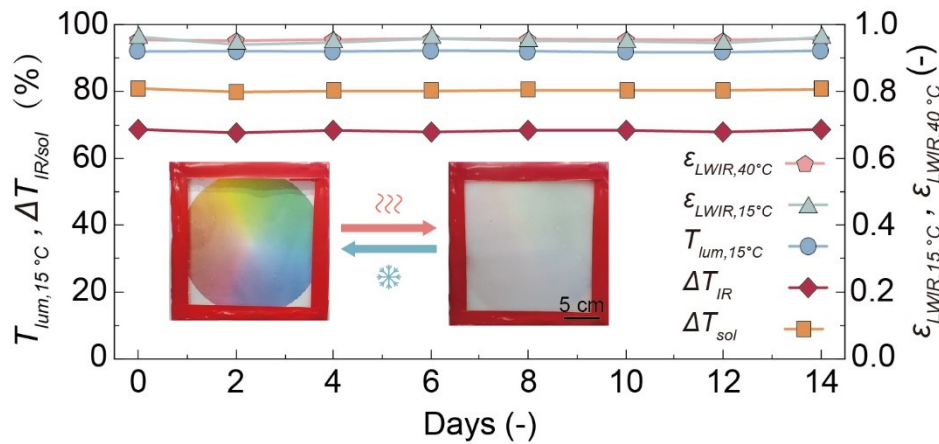
5 **Figure S19.** Differential scanning calorimetry (DSC) curves to track the thermal  
6 affects of FIRIST hydrogel in a heating and cooling cycle. Prior to measurement, the  
7 thermal history of this sample was removed by heating treatment in water at 40 °C.



1

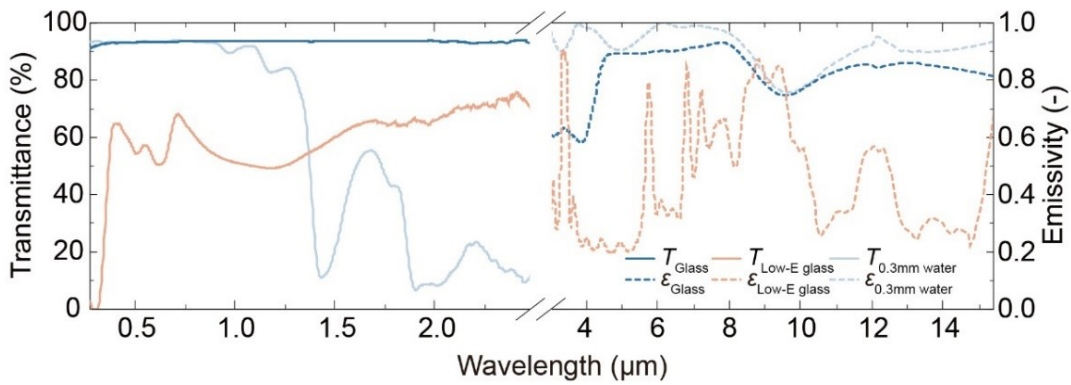
2 **Figure S20. Cycling testing for the FIRST smart window.** a The 3D modeling  
 3 diagram of the cyclic testing device (**Figure S20aI**) and the actual construction of the  
 4 finished product display of the cyclic testing device (**Figure S20aII**). b Optical  
 5 performance of FIRST hydrogels during cyclic testing. As shown in **Figure S20b**, the  
 6 major performance index of FIRST smart window at both 15 °C and 40 °C were almost  
 7 constant after 500 cycles. In the cyclic test system, we used a DC power supply to  
 8 supply current, a relay to control circuit switching, and a pulse generator to control  
 9 circuit switching time, multi-channel data recorder with external semiconductor  
 10 refrigeration plate is responsible for cooling, and ITO conductive glass is linked to DC  
 11 power supply and stacked below the smart window for heating. We set a heating time

1 of 15 s and a cooling time of 120 s.



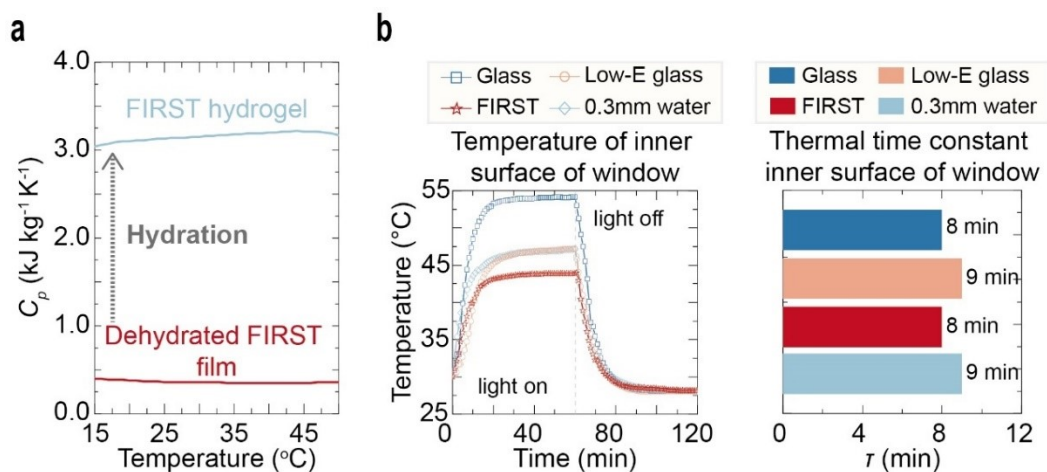
2

3 **Figure S21.** Optical modulation performance of FIRST smart window over 14 days.



4

5 **Figure S22.** Transmittance/Emissivity spectra for the glass, low-E glass, and 0.3 mm water.  
6



7

8 **Figure S23. Thermal properties of FIRST hydrogel-based thermochromic**  
9 **windows.** **a** specific heat capacity of FIRST hydrogel (light blue line) and dry PVB  
10 **film** (red line). **b** Temperature of the inner surface in Case I of the window  
11 (temperature reading of thermometer A) with respect to the lighting time for the  
12 glass, 0.1mm water, Low-E glass, and FIRST hydrogel, respectively. (left). Air

1 temperature in the device (temperature reading of thermometer B) with respect to the  
 2 lighting time for glass, 0.1mm water, Low-E glass, and FIRST hydrogel,  
 3 respectively. (right). **c** Thermal time constant ( $\tau$ ) of the inner surface in **Case III**.

4 **Table S10. Light and thermal regulation properties of different hydrogel systems.**

Material	$T_{lum}$ (%)	$\Delta T_{IR}$ (%)	$\Delta T_{sol}$ (%)	Thickness ( $\mu\text{m}$ )	Response time (min)	Reference
PNIPAm-Hydrogel	89.1	49.2	69.1	200	NA <sup>a</sup>	73
PNIPAm-Solution	90.0	41.0	68.1	10000	15.00 <sup>b</sup>	1
PU/POSS hydrogel	99.0	40.0	51.0	200	1.00 <sup>c</sup>	15
PNIPAm/water/glycero l hydrogel	89.2	48.0	60.8	400	0.16 <sup>d</sup>	39
P(NIPAM-AEMA)	87.2	75.6	81.3	240	5.00 <sup>b</sup>	2
HPC/NaCl hydrogel	88.5	16.4	40.1	350	NA <sup>a</sup>	74
$V^{O_2}$ /PNIPAM hybrid hydrogel	82.1	29.9	34.7	52	NA <sup>a</sup>	7
HPCA/W- $V^{O_2}$ hydrogel	79.0	24.0	36.4	25	NA <sup>a</sup>	75
HPC hydrogel	71.6	37.7	50.4	150	5.00 <sup>d</sup>	56
C-g-PDN solution	95.7	52.0	76.0	10000	5.33 <sup>f</sup>	76
HPC/PAA Hybrid Hydrogel	90.1	37.0	47.5	1000	1.4 <sup>e</sup>	43
PNIPAm/ $V^{O_2}@Si^{O_2}$ hydrogel	37.0	NA <sup>a</sup>	63.0	NA <sup>a</sup>	NA <sup>a</sup>	8
HPMC/AuNCs hydrogel	88.9	36.0	62.6	NA <sup>a</sup>	3.00 <sup>c</sup>	75
$Cu_7S_4$ /PNIPAm Composite Hydrogel	79.0	27.0	32.0	75	2.00 <sup>c</sup>	78
P(NIPAm-co-DMAA)	91.30	NA <sup>a</sup>	88.8	1000	NA <sup>a</sup>	37
FIRST	92.4	68.5	80.8	300	0.16 <sup>d</sup>	This work

5 <sup>a</sup> No available data was reported in relevant literature.

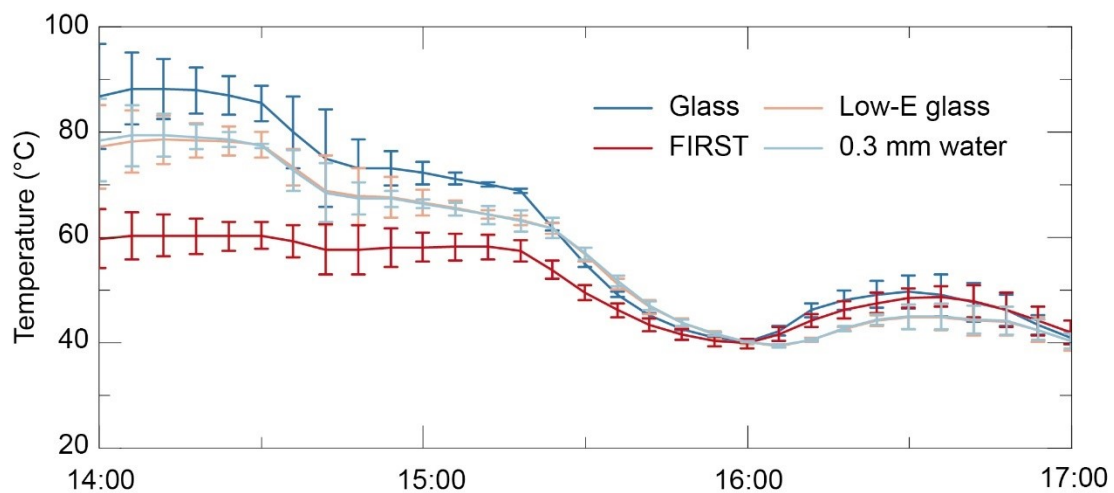
6 <sup>b</sup> Phase transition induced by Xenon lamp irradiation heating.

7 <sup>c</sup> Phase transition induced by exposure to direct sunlight.

8 <sup>d</sup> Phase Transition induced by thermal stimulation.

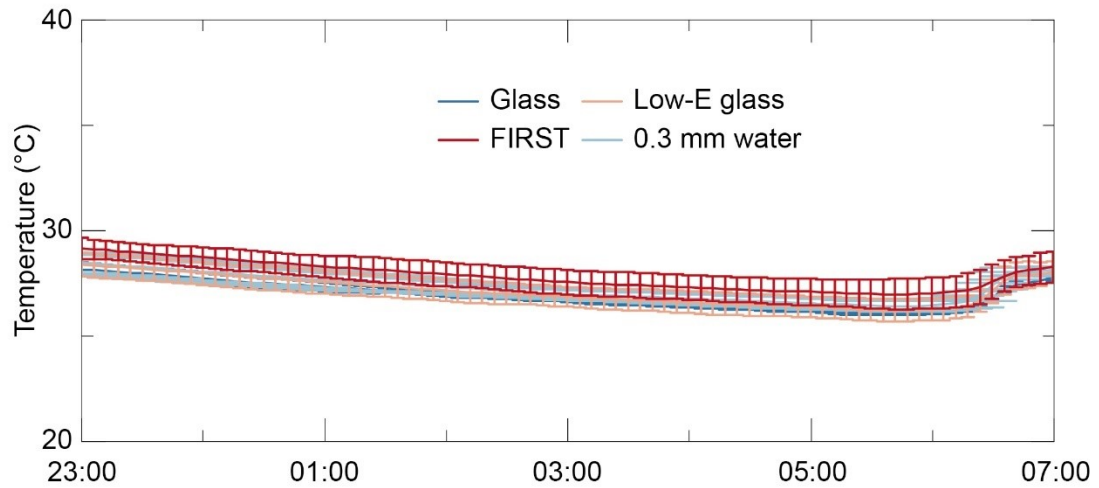
9 <sup>e</sup> Phase Transition induced by heating.

1 f Phase transition induced by near infrared light source irradiation heating.  
 2  
 3 It's also crucial to underscore that, in the majority of existing literatures, the assessment  
 4 of thermochromic window "performance" is conventionally conducted at the device  
 5 level. At present, the exploration of thermochromic windows remains in its early  
 6 developmental phases. A standardized protocol for performance evaluation has not yet  
 7 been established. Thus, exercising caution when making "comparisons" between  
 8 various devices is paramount. For instance, comparisons involving metrics like  
 9 luminous transmittance ( $T_{lum}$ ) and solar modulation ( $\Delta T_{sol}$ ) may entail devices  
 10 incorporating diverse thicknesses of active materials. Similarly, assessing response  
 11 time might involve different illumination or heating sources, potentially resulting in  
 12 significant variations in temperature gradients. In this work, in order to better fit the  
 13 real life use scenario, we use the method of thermal stimulation to measure the response  
 14 time of the intelligent window<sup>77</sup>.



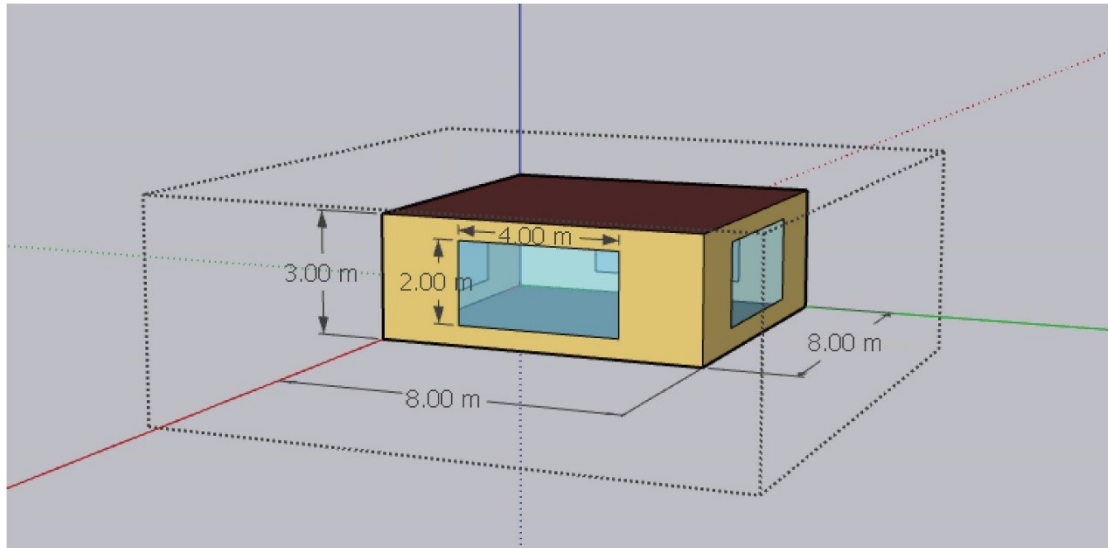
15  
 16 **Figure S24. 13:00-17:00 air temperature curve for the outdoor demonstration in**  
 17 **Guangzhou.** As shown in **Figure S24** and **Figure 5f**, in general, when the outdoor  
 18 temperature in summer reaches the hottest time of the day (14:00), the temperature of  
 19 ordinary glass should be the highest. In this test, also as expected, the geometric center  
 20 temperature of ordinary glass reached 86.7 °C at 14:00, and the geometric center of  
 21 0.3mm thick water and Low-E glass decreased in order, while the geometric  
 22 temperature of FIRST was only 59.6 °C, the lowest among the four windows.

23  
 24



1 23:00 01:00 03:00 05:00 07:00  
 2 **Figure S25. 00:00-06:00 air temperature curve for the outdoor demonstration in**  
 3 **Guangzhou.** In the early morning hours of summer in Guangzhou, the temperature  
 4 difference between the geometric centers of the four windows is not very large, all in  
 5 the range of 26.9 °C to 27.9 °C.

6  
 7  
 8  
 9  
 10  
 11  
 12  
 13  
 14  
 15  
 16



1

2 **Figure S26. The house model for simulation.** An 8 m by 8 m by 3 m model house  
3 with four 2 m by 4 m windows in the center of four walls was built in EnergyPlus. glass  
4 panel, Low-E glass and FIRST hydrogel were calculated separately, with optical data  
5 shown in **Table S11** for the three windows. The internal heat loads were calculated on  
6 the basis of the house are. Two people and total power of 6 W/m<sup>2</sup> from electronic and  
7 electrical devices were considered as internal heat loads. Climate data of Anchorage,  
8 Guangzhou, Beijing, Wuhan, and Chongqing were selected to analyze the window  
9 performance in different city in China. The indoor thermal regulation by the smart  
10 windows was recorded through the simulation without an HVAC system, while the  
11 energy-saving assessment was proceeded by adding an HVAC system with a single set  
12 point of 26 °C and recording the energy consumption for both heating and cooling of  
13 each model.

14

15

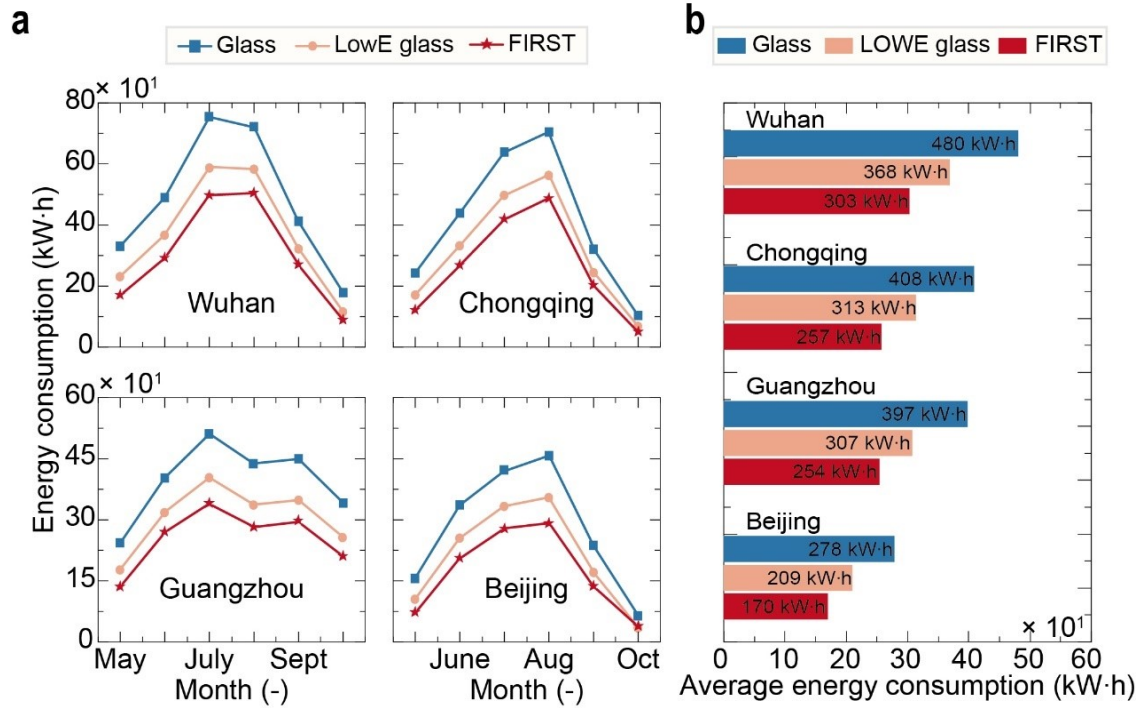
16

17

18

19

20



1

2 **Figure S27. Energyplus energy simulation for plain glass, Low-E glass and FIRST**  
 3 **smart windows. a** EnergyPlus refrigeration energy consumption simulation in four  
 4 **cities of China. b** Average energy consumption simulation in a.

5

6

**Table S11. Optical data of different windows.**

	Glass	Low-E glass	0.3 mm water	FIRST hydrogel
Thickness (mm)	10	10	10	0.3
$T_{sol}$ (%)	93.4	56.4	86.9	89.8 (cool)/9.0 (hot)
$T_{IR}$ (%)	93.5	56.3	76.4	87.1 (cool)/18.6 (hot)
$T_{lum}$ (%)	93.2	58.4	94.8	90.7 (cool)/ 9.0 (hot)
$\varepsilon_{LWIR}$ (-)	0.82	0.57	0.86	0.96 (cool)/0.95 (hot)

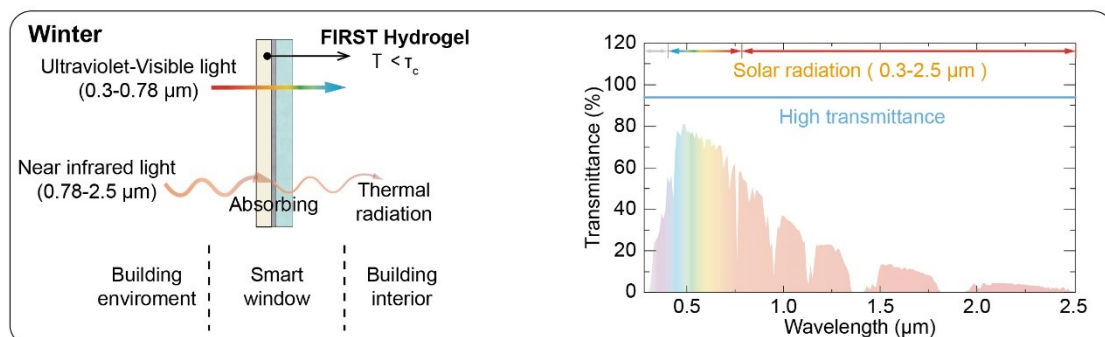
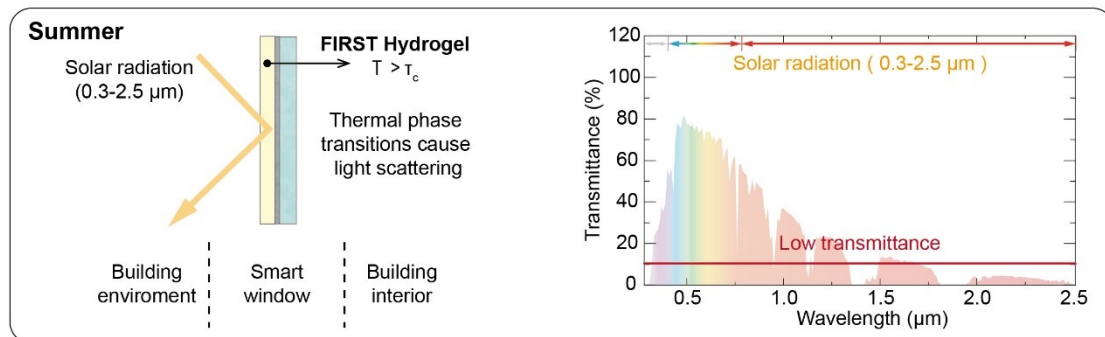
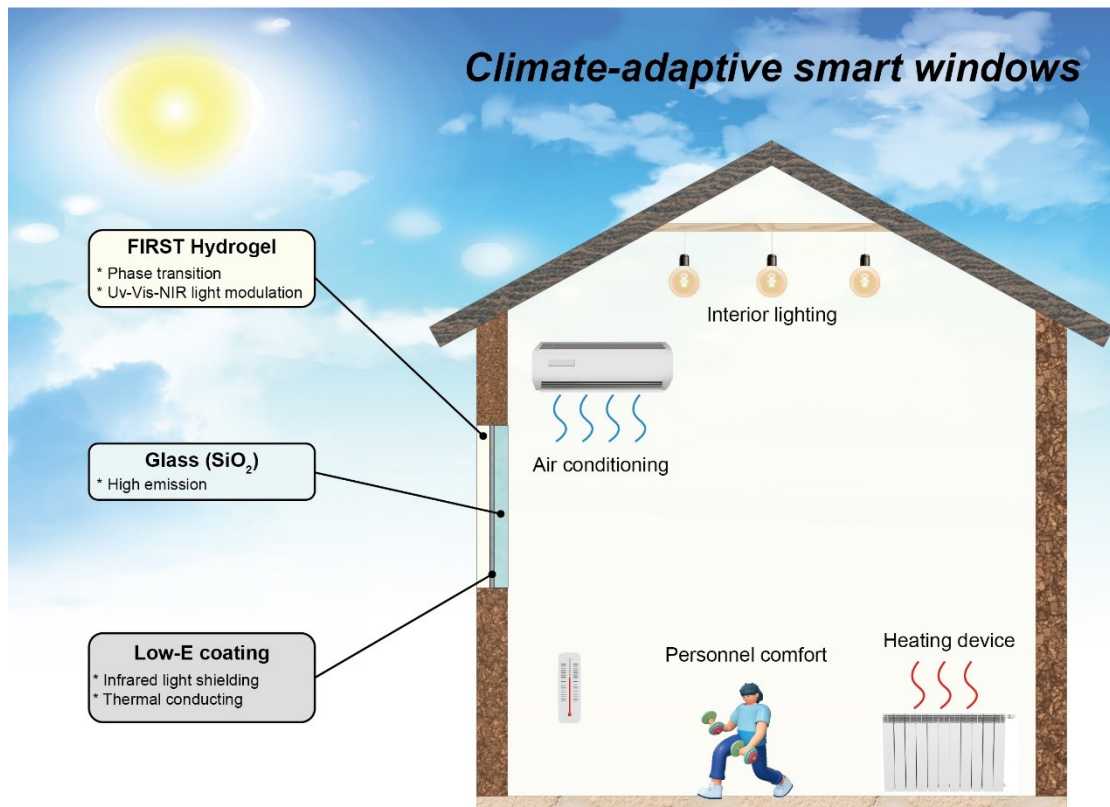
7

8

9

10

11



2

3 **Figure S28. Concept of all-weather thermochromic windows composed of stacked**  
 4 **FIRST hydrogel layer and Low-e glass.** During the summer months, the initial layer  
 5 (FIRST) transitions to an opaque state, reflecting visible and near-infrared photons back  
 6 into the external environment. In the winter months, the FIRST layer absorbs near-  
 7 infrared radiation from the sun, leveraging the effective near-infrared light absorption

1 capability of water. The absorbed near-infrared light is converted into heat, which is  
2 subsequently conducted to the glass through the Low-E layer, known for its high  
3 thermal conductivity. The absorbed heat can then be re-emitted into the room through  
4 the glass, facilitated by the high emissivity of SiO<sub>2</sub>.<sup>80</sup> Note that the reverse process,  
5 namely the emitting heat inside buildings into the external environment, cannot occur  
6 due to the existence of Low-e layer.

7

8

## 9 (IV) Supplementary References:

- 10 1. Zhou, Y.; Wang, S.; Peng, J.; Tan, Y.; Li, C.; Boey, F. Y. C.; Long, Y., Liquid thermo-  
11 responsive smart window derived from hydrogel. *Joule* **2020**, *4* (11), 2458-2474.
- 12 2. Li, X.-H.; Liu, C.; Feng, S.-P.; Fang, N. X., Broadband light management with thermochromic  
13 hydrogel microparticles for smart windows. *Joule* **2019**, *3* (1), 290-302.
- 14 3. Chen, G.; Wang, K.; Yang, J.; Huang, J.; Chen, Z.; Zheng, J.; Wang, J.; Yang, H.; Li,  
15 S.; Miao, Y.; Wang, W.; Zhu, N.; Jiang, X.; Chen, Y.; Fu, J., Printable Thermochromic  
16 Hydrogel-Based Smart Window for All-Weather Building Temperature Regulation in Diverse Climates.  
17 *Advanced Materials* **2023**, *35* (20), 2211716.
- 18 4. Guo, H.; Sanson, N.; Marcellan, A.; Hourdet, D., Thermoresponsive toughening in LCST-type  
19 hydrogels: Comparison between semi-interpenetrated and grafted networks. *Macromolecules* **2016**, *49*  
20 (24), 9568-9577.
- 21 5. Guo, H.; Sanson, N.; Hourdet, D.; Marcellan, A., Thermoresponsive Toughening with Crack  
22 Bifurcation in Phase-Separated Hydrogels under Isochoric Conditions. *Advanced Materials* **2016**, *28*  
23 (28), 5857-5864.
- 24 6. Mu, J.; Zheng, S., Poly (N-isopropylacrylamide) nanocrosslinked by polyhedral oligomeric  
25 silsesquioxane: temperature-responsive behavior of hydrogels. *Journal of colloid and interface science*  
26 **2007**, *307* (2), 377-385.
- 27 7. Zhou, Y.; Cai, Y.; Hu, X.; Long, Y., VO<sub>2</sub>/hydrogel hybrid nanothermochromic material with  
28 ultra-high solar modulation and luminous transmission. *Journal of Materials Chemistry A* **2015**, *3* (3),  
29 1121-1126.
- 30 8. Ke, Y.; Zhou, C.; Zhou, Y.; Wang, S.; Chan, S. H.; Long, Y., Emerging thermal-responsive  
31 materials and integrated techniques targeting the energy-efficient smart window application. *Advanced*  
32 *functional materials* **2018**, *28* (22), 1800113.
- 33 9. Mao, J.; Yu, Q. J.; Wang, S., Preparation of multifunctional hydrogels with pore channels using  
34 agarose sacrificial templates and its applications. *Polymers for Advanced Technologies* **2021**, *32* (4),  
35 1752-1762.
- 36 10. Yu, Q. J.; Mao, J.; Wang, S.; Guo, Z. Y., A simple multifunctional PNIPAM-GO/PANI hydrogel  
37 preparation strategy and its application in dye adsorption and infrared switching. *Journal of*  
38 *Macromolecular Science, Part A* **2020**, *57* (11), 751-760.
- 39 11. Feng, Y.; Wang, S.; Li, Y.; Ma, W.; Zhang, G.; Yang, M.; Li, H.; Yang, Y.; Long, Y.,

1 Entanglement in Smart Hydrogels: Fast Response Time, Anti-Freezing and Anti-Drying. *Advanced*  
2 *Functional Materials* **2023**, 33 (21), 2211027.

3 12. Yang, X.; Li, Z.; Liu, H.; Ma, L.; Huang, X.; Cai, Z.; Xu, X.; Shang, S.; Song, Z.,  
4 Cellulose-based polymeric emulsifier stabilized poly (N-vinylcaprolactam) hydrogel with temperature  
5 and pH responsiveness. *International journal of biological macromolecules* **2020**, 143, 190-199.

6 13. Matsubara, K.; Watanabe, M.; Takeoka, Y., A Thermally Adjustable Multicolor Photochromic  
7 Hydrogel. *Angewandte Chemie International Edition* **2007**, 46 (10), 1688-1692.

8 14. Nonoyama, T.; Lee, Y. W.; Ota, K.; Fujioka, K.; Hong, W.; Gong, J. P., Instant thermal  
9 switching from soft hydrogel to rigid plastics inspired by thermophile proteins. *Advanced Materials*  
10 **2020**, 32 (4), 1905878.

11 15. Zhang, Q.; Jiang, Y.; Chen, L.; Chen, W.; Li, J.; Cai, Y.; Ma, C.; Xu, W.; Lu, Y.;  
12 Jia, X., Ultra-compliant and tough thermochromic polymer for self-regulated smart windows. *Advanced*  
13 *Functional Materials* **2021**, 31 (18), 2100686.

14 16. Shi, K.; Liu, Z.; Yang, C.; Li, X.-Y.; Sun, Y.-M.; Deng, Y.; Wang, W.; Ju, X.-J.; Xie,  
15 R.; Chu, L.-Y., Novel Biocompatible Thermoresponsive Poly(N-vinyl Caprolactam)/Clay  
16 Nanocomposite Hydrogels with Macroporous Structure and Improved Mechanical Characteristics. *ACS*  
17 *Applied Materials & Interfaces* **2017**, 9 (26), 21979-21990.

18 17. Niu, Y.; Zhou, Y.; Du, D.; Ouyang, X.; Yang, Z.; Lan, W.; Fan, F.; Zhao, S.; Liu,  
19 Y.; Chen, S.; Li, J.; Xu, Q., Energy Saving and Energy Generation Smart Window with Active  
20 Control and Antifreezing Functions. *Advanced Science* **2022**, 9 (6), 2105184.

21 18. Xu, Z.; Wang, S.; Hu, X. Y.; Jiang, J.; Sun, X.; Wang, L., Sunlight-induced  
22 photo-thermochromic supramolecular nanocomposite hydrogel film for energy-saving smart window.  
23 *Solar Rrl* **2018**, 2 (11), 1800204.

24 19. Liu, Y.; Guo, Y.; Zhang, Z.; Huang, Z.; Qi, P.; Cui, J.; Song, A.; Hao, J., A new  
25 application of Krafft point concept: an ultraviolet-shielded surfactant switchable window. *Chemical*  
26 *Communications* **2020**, 56 (39), 5315-5318.

27 20. Li, K.; Meng, S.; Xia, S.; Ren, X.; Gao, G., Durable and controllable smart windows based on  
28 thermochromic hydrogels. *ACS Applied Materials & Interfaces* **2020**, 12 (37), 42193-42201.

29 21. Xu, G.; Xia, H.; Chen, P.; She, W.; Zhang, H.; Ma, J.; Ruan, Q.; Zhang, W.; Sun, Z.,  
30 Thermochromic Hydrogels with Dynamic Solar Modulation and Regulatable Critical Response  
31 Temperature for Energy-Saving Smart Windows. *Advanced Functional Materials* **2022**, 32 (5), 2109597.

32 22. Yu, Z.; Yang, Y.; Shen, C.; Mao, L.; Cui, C.; Chen, Z.; Zhang, Y., Thermochromic  
33 hydrogels with an adjustable critical response temperature for temperature monitoring and smart  
34 windows. *Journal of Materials Chemistry C* **2023**, 11 (2), 583-592.

35 23. Zhou, Y.; Dong, X.; Mi, Y.; Fan, F.; Xu, Q.; Zhao, H.; Wang, S.; Long, Y., Hydrogel  
36 smart windows. *Journal of Materials Chemistry A* **2020**, 8 (20), 10007-10025.

37 24. Yuan, N.; Xu, L.; Wang, H.; Fu, Y.; Zhang, Z.; Liu, L.; Wang, C.; Zhao, J.; Rong, J.,  
38 Dual physically cross-linked double network hydrogels with high mechanical strength, fatigue resistance,  
39 notch-insensitivity, and self-healing properties. *ACS Applied Materials & Interfaces* **2016**, 8 (49), 34034-  
40 34044.

41 25. Tuncaboylu, D. C.; Sari, M.; Oppermann, W.; Okay, O., Tough and self-healing hydrogels  
42 formed via hydrophobic interactions. *Macromolecules* **2011**, 44 (12), 4997-5005.

- 1 26. Wang, F.; Yong, X.; Deng, J.; Wu, Y., Poly (N, N-dimethylacrylamide-octadecyl acrylate)-clay  
2 hydrogels with high mechanical properties and shape memory ability. *RSC advances* **2018**, *8* (30),  
3 16773-16780.
- 4 27. Su, Q.; Wang, Y.; Guan, S.; Zhang, H.; Gao, G. H.; Zhu, X., Rapid formation of highly  
5 stretchable and notch-insensitive hydrogels. *RSC advances* **2016**, *6* (36), 30570-30576.
- 6 28. Kurt, B.; Gulyuz, U.; Demir, D. D.; Okay, O., High-strength semi-crystalline hydrogels with  
7 self-healing and shape memory functions. *European Polymer Journal* **2016**, *81*, 12-23.
- 8 29. Gulyuz, U.; Okay, O., Self-healing polyacrylic acid hydrogels. *Soft Matter* **2013**, *9* (43), 10287-  
9 10293.
- 10 30. Wang, F.; Weiss, R., Thermoresponsive supramolecular hydrogels with high fracture toughness.  
11 *Macromolecules* **2018**, *51* (18), 7386-7395.
- 12 31. Meng, L.; Shao, C.; Cui, C.; Xu, F.; Lei, J.; Yang, J., Autonomous self-healing silk fibroin  
13 injectable hydrogels formed via surfactant-free hydrophobic association. *ACS applied materials &*  
14 *interfaces* **2019**, *12* (1), 1628-1639.
- 15 32. Pan, J.; Zeng, H.; Gao, L.; Zhang, Q.; Luo, H.; Shi, X.; Zhang, H., Hierarchical multiscale  
16 hydrogels with identical compositions yet disparate properties via tunable phase separation. *Advanced*  
17 *Functional Materials* **2022**, *32* (13), 2110277.
- 18 33. Pan, J.; Zhang, W.; Zhu, J.; Tan, J.; Huang, Y.; Mo, K.; Tong, Y.; Xie, Z.; Ke, Y.;  
19 Zheng, H., Arrested Phase Separation Enables High-Performance Keratoprostheses. *Advanced Materials*  
20 **2023**, *35* (16), 2207750.
- 21 34. Prange, M. M.; Hooper, H. H.; Prausnitz, J. M., Thermodynamics of aqueous systems containing  
22 hydrophilic polymers or gels. *AIChE journal* **1989**, *35* (5), 803-813.
- 23 35. Müller, M.; Abetz, V., Nonequilibrium processes in polymer membrane formation: Theory and  
24 experiment. *Chemical Reviews* **2021**, *121* (22), 14189-14231.
- 25 36. Chen, L.; Zhao, C.; Huang, J.; Zhou, J.; Liu, M., Enormous-stiffness-changing polymer  
26 networks by glass transition mediated microphase separation. *Nature Communications* **2022**, *13* (1),  
27 6821.
- 28 37. Chen, G.; Wang, K.; Yang, J.; Huang, J.; Chen, Z.; Zheng, J.; Wang, J.; Yang, H.; Li,  
29 S.; Miao, Y., Printable Thermochromic Hydrogel-Based Smart Window for All-Weather Building  
30 Temperature Regulation in Diverse Climates. *Advanced Materials* **2023**, 2211716.
- 31 38. Matsubara, K.; Watanabe, M.; Takeoka, Y., A thermally adjustable multicolor photochromic  
32 hydrogel. *Angewandte Chemie* **2007**, *119* (10), 1718-1722.
- 33 39. Li, G.; Chen, J.; Yan, Z.; Wang, S.; Ke, Y.; Luo, W.; Ma, H.; Guan, J.; Long, Y.,  
34 Physical crosslinked hydrogel-derived smart windows: anti-freezing and fast thermal responsive  
35 performance. *Materials Horizons* **2023**.
- 36 40. Ding, Y.; Duan, Y.; Yang, F.; Xiong, Y.; Guo, S., High-transmittance pNIPAm gel smart  
37 windows with lower response temperature and stronger solar regulation. *Chemical Engineering Journal*  
38 **2023**, *460*, 141572.
- 39 41. Nakamura, A.; Ogai, R.; Murakami, K., Development of smart window using an hydroxypropyl  
40 cellulose-acrylamide hydrogel and evaluation of weathering resistance and heat shielding effect. *Solar*  
41 *Energy Materials and Solar Cells* **2021**, *232*, 111348.
- 42 42. Niu, Y.; Zhou, Y.; Du, D.; Ouyang, X.; Yang, Z.; Lan, W.; Fan, F.; Zhao, S.; Liu,

1 Y.; Chen, S., Energy saving and energy generation smart window with active control and antifreezing  
2 functions. *Advanced Science* **2022**, *9* (6), 2105184.

3 43. Zhang, L.; Xia, H.; Xia, F.; Du, Y.; Wu, Y.; Gao, Y., Energy-saving smart windows with  
4 HPC/PAA hybrid hydrogels as thermochromic materials. *ACS Applied Energy Materials* **2021**, *4* (9),  
5 9783-9791.

6 44. Nakamura, C.; Yamamoto, T.; Manabe, K.; Nakamura, T.; Einaga, Y.; Shiratori, S.,  
7 Thermoresponsive, freezing-resistant smart windows with adjustable transition temperature made from  
8 hydroxypropyl cellulose and glycerol. *Industrial & Engineering Chemistry Research* **2019**, *58* (16),  
9 6424-6428.

10 45. Shi, K.; Liu, Z.; Yang, C.; Li, X.-Y.; Sun, Y.-M.; Deng, Y.; Wang, W.; Ju, X.-J.; Xie,  
11 R.; Chu, L.-Y., Novel biocompatible thermoresponsive poly (N-vinyl caprolactam)/clay nanocomposite  
12 hydrogels with macroporous structure and improved mechanical characteristics. *ACS applied materials*  
13 *& interfaces* **2017**, *9* (26), 21979-21990.

14 46. Timaeva, O.; Kuz'Micheva, G.; Pashkin, I.; Czakkel, O.; Prevost, S., Structure and dynamics  
15 of titania–poly (N-vinyl caprolactam) composite hydrogels. *Soft Matter* **2020**, *16* (1), 219-228.

16 47. Li, K.; Gao, H.; Ren, X.; Gao, G. Regulatable thermochromic hydrogels via hydrogen bonds driven  
17 by potassium tartrate hemihydrate. *ACS sustainable chemistry & engineering* **2019**, *7* (17), 15036-15043.

18 48. Meco, E.; Lampe, K. J. Impact of elastin-like protein temperature transition on PEG-ELP hybrid  
19 hydrogel properties. *Biomacromolecules* **2019**, *20* (5), 1914-1925.

20 49. Lee, H. Y.; Cai, Y.; Velioglu, S.; Mu, C.; Chang, C. J.; Chen, Y. L.; Song, Y.; Chew,  
21 J. W.; Hu, X. M., Thermochromic Ionogel: A New Class of Stimuli Responsive Materials with Super  
22 Cyclic Stability for Solar Modulation. *Chemistry of Materials* **2017**, *29* (16), 6947-6955.

23 50. Timaeva, O. I.; Kuz'micheva, G. M.; Pashkin, I. I.; Czakkel, O.; Prevost, S., Structure and  
24 dynamics of titania – poly(N-vinyl caprolactam) composite hydrogels. *Soft Matter* **2020**, *16* (1), 219-  
25 228.

26 51. Gao, J.; Frisken, B. J., Cross-Linker-Free N-Isopropylacrylamide Gel Nanospheres. *Langmuir*  
27 **2003**, *19* (13), 5212-5216.

28 52. Brugnoli, M.; Nickel, A. C.; Kröger, L. C.; Scotti, A.; Pich, A.; Leonhard, K.; Richtering,  
29 W., Synthesis and structure of deuterated ultra-low cross-linked poly(N-isopropylacrylamide) microgels.  
30 *Polymer Chemistry* **2019**, *10* (19), 2397-2405.

31 53. Cooperstein, M. A.; Canavan, H. E., Assessment of cytotoxicity of (N-isopropyl acrylamide) and  
32 Poly(N-isopropyl acrylamide)-coated surfaces. *Biointerphases* **2013**, *8* (1).

33 54. Tang, L.; Wang, L.; Yang, X.; Feng, Y.; Li, Y.; Feng, W., Poly (N-isopropylacrylamide)-  
34 based smart hydrogels: Design, properties and applications. *Progress in Materials Science* **2021**, *115*,  
35 100702.

36 55. Connelly, K.; Wu, Y.; Chen, J.; Lei, Y., Design and development of a reflective membrane for  
37 a novel Building Integrated Concentrating Photovoltaic (BICPV)‘Smart Window’ system. *Applied*  
38 *energy* **2016**, *182*, 331-339.

39 56. Wang, S.; Zhou, Y.; Jiang, T.; Yang, R.; Tan, G.; Long, Y., Thermochromic smart windows  
40 with highly regulated radiative cooling and solar transmission. *Nano Energy* **2021**, *89*, 106440.

41 57. Ogawa, A.; Nakayama, S.; Uehara, M.; Mori, Y.; Takahashi, M.; Aiba, T.; Kurosaki, Y.,  
42 Pharmaceutical properties of a low-substituted hydroxypropyl cellulose (L-HPC) hydrogel as a novel

1 external dressing. *International Journal of Pharmaceutics* **2014**, 477 (1-2), 546-552.

2 58. Jain, S.; Sandhu, P. S.; Malvi, R.; Gupta, B., Cellulose derivatives as thermoresponsive polymer:  
3 an overview. *Journal of applied pharmaceutical science* **2013**, 3 (12), 139-144.

4 59. Kabir, S. F.; Sikdar, P. P.; Haque, B.; Bhuiyan, M. R.; Ali, A.; Islam, M., Cellulose-based  
5 hydrogel materials: Chemistry, properties and their prospective applications. *Progress in biomaterials*  
6 **2018**, 7, 153-174.

7 60. Sala, R. L.; Goncalves, R. H.; Camargo, E. R.; Leite, E. R., Thermosensitive poly (N-  
8 vinylcaprolactam) as a transmission light regulator in smart windows. *Solar Energy Materials and Solar*  
9 *Cells* **2018**, 186, 266-272.

10 61. Halligan, S. C.; Dalton, M. B.; Murray, K. A.; Dong, Y.; Wang, W.; Lyons, J. G.; Geever,  
11 L. M., Synthesis, characterisation and phase transition behaviour of temperature-responsive physically  
12 crosslinked poly (N-vinylcaprolactam) based polymers for biomedical applications. *Materials Science*  
13 *and Engineering: C* **2017**, 79, 130-139.

14 62. Chen, Z.; Chen, Y.; Guo, Y.; Yang, Z.; Li, H.; Liu, H., Paper-structure inspired  
15 multiresponsive hydrogels with solvent-induced reversible information recording, self-encryption, and  
16 multidecryption. *Advanced Functional Materials* **2022**, 32 (23), 2201009.

17 63. Hu, Y.; Barbier, L.; Li, Z.; Ji, X.; Le Blay, H.; Hourdet, D.; Sanson, N.; Lam, J. W.;  
18 Marcellan, A.; Tang, B. Z., Hydrophilicity-hydrophobicity transformation, thermoresponsive  
19 morphomechanics, and crack multifurcation revealed by AIEgens in mechanically strong hydrogels.  
20 *Advanced Materials* **2021**, 33 (39), 2101500.

21 64. Hiroki, A.; Taguchi, M., Development of environmentally friendly cellulose derivative-based  
22 hydrogels for contact lenses using a radiation crosslinking technique. *Applied Sciences* **2021**, 11 (19),  
23 9168.

24 65. Zavgorodnya, O.; Kozlovskaya, V.; Liang, X.; Kothalawala, N.; Catledge, S. A.; Dass, A.;  
25 Kharlampieva, E., Temperature-responsive properties of poly (N-vinylcaprolactam) multilayer  
26 hydrogels in the presence of Hofmeister anions. *Materials Research Express* **2014**, 1 (3), 035039.

27 66. Zhuo, S.; Halligan, E.; Tie, B. S. H.; Breheny, C.; Geever, L. M., Lower Critical Solution  
28 Temperature Tuning and Swelling Behaviours of NVCL-Based Hydrogels for Potential 4D Printing  
29 Applications. *Polymers* **2022**, 14 (15), 3155.

30 67. Wang, C.; Luan, W.; Zeng, Z.; Wang, H.; Sun, L.; Wang, J. H., Polyvinyl Butyral with  
31 Different Acetalization Degrees: Synthesis and Solubility Parameters. *Journal of Macromolecular*  
32 *Science, Part B* **2022**, 61 (1), 92-110.

33 68. Lin, X.; Wang, K.; Zhou, B.; Luo, G., A microreactor-based research for the kinetics of polyvinyl  
34 butyral (PVB) synthesis reaction. *Chemical Engineering Journal* **2020**, 383, 123181.

35 69. Rong-zhen, Z.; Zhi-bin, W.; Ke-wu, L.; You-hua, C., Study on Refractive Index Characteristics  
36 of Chitosan Hydrogel. *SPECTROSCOPY AND SPECTRAL ANALYSIS* **2020**, 40 (6), 1846-1851.

37 70. Wang, S.; Liu, M.; Gao, L.; Guo, G.; Huo, Y., Optimized association of short alkyl side chains  
38 enables stiff, self-recoverable, and durable shape-memory hydrogel. *ACS applied materials & interfaces*  
39 **2019**, 11 (21), 19554-19564.

40 71. Panyukov, S.; Rabin, Y., Polymer gels: frozen inhomogeneities and density fluctuations.  
41 *Macromolecules* **1996**, 29 (24), 7960-7975.

42 72. Nigro, V.; Angelini, R.; Bertoldo, M.; Buratti, E.; Franco, S.; Ruzicka, B., Chemical-physical

1 behaviour of microgels made of interpenetrating polymer networks of PNIPAM and poly (acrylic acid).  
2 *Polymers* **2021**, *13* (9), 1353.

3 73. Zhou, Y.; Cai, Y.; Hu, X.; Long, Y., Temperature-responsive hydrogel with ultra-large solar  
4 modulation and high luminous transmission for “smart window” applications. *Journal of Materials*  
5 *Chemistry A* **2014**, *2* (33), 13550-13555.

6 74. Chiang, F. B., Temperature-responsive hydroxypropylcellulose based thermochromic material and  
7 its smart window application. *RSC advances* **2016**, *6* (66), 61449-61453.

8 75. Yang, Y.-S.; Zhou, Y.; Chiang, F. B. Y.; Long, Y., Tungsten doped VO<sub>2</sub>/microgels hybrid  
9 thermochromic material and its smart window application. *RSC advances* **2017**, *7* (13), 7758-7762.

10 76. Tan, Y.; Chen, R.; Xiao, Y.; Wang, C.; Zhou, C.; Chen, D.; Li, S.; Wang, W., Temperature-  
11 responsive ‘cloud’ with controllable self-assembled particle size for smart window application. *Applied*  
12 *Materials Today* **2021**, *25*, 101248.

13 77. Cao, D.; Xu, C.; Lu, W.; Qin, C.; Cheng, S., Sunlight-Driven Photo-Thermochromic Smart  
14 Windows. *Solar Rrl* **2018**, *2* (4), 1700219.

15 78. Zhu, H.; Wang, L., Smart window based on Cu<sub>7</sub>S<sub>4</sub>/hydrogel composites with fast photothermal  
16 response. *Solar Energy Materials and Solar Cells* **2019**, *202*, 110109.

17 79. Peng, H.; Yang, X.; Gu, Y.; Yang, Q.; Lan, T.; Chen, S.; Yan, B. Thermochromic smart windows  
18 with broad-range customizable responsive temperature via the Hofmeister effect. *Journal of Materials*  
19 *Chemistry A* **2023**, *11* (33), 17848-17857.

20 80. Youngblood, N.; Talagrand, C.; Porter, B. F.; Galante, C. G.; Kneepkens, S.; Triggs, G.;  
21 Ghazi Sarwat, S.; Yarmolich, D.; Bonilla, R. S.; Hosseini, P.; Taylor, R. A.; Bhaskaran, H.,  
22 Reconfigurable Low-Emissivity Optical Coating Using Ultrathin Phase Change Materials. *ACS*  
23 *Photonics* **2022**, *9* (1), 90-100.

24